Observations of NGC1068 with DESHIMA 2.0

verifying the science capabilities of the integrated superconducting spectrometer

Michiel J. Endtz

Technische Universiteit Delft

TU Delft

Observations of NGC1068 with DESHIMA 2.0

verifying the science capabilities of the integrated superconducting spectrometer

by

Michiel J. Endtz

to obtain the degree of Bachelor of Science
in Applied Physics at the Delft University of Technology

Student number:	5876389
Project duration:	April 22, 2025 – June 27, 2025
Supervisor:	Akira Endo
Examiner:	Iman Esmaeil Zadeh
	2nd examiner
Study programme:	Bachelor of Applied Sciences
Faculty:	Faculty of applied sciences
Cover:	A photograph of the Aste telescope in the Atacama Desert in Chile

TU Delft

Abstract

The single-pixel integrated superconducting spectrometer DESHIMA 2.0 on 10 m Atacama Submillimeter Telescope Experiment (ASTE) aims to provide broadband spectra from 200 to 400 GHz at medium resolution. This spectral range enables observations of (sub) millimetre-wave astronomy, especially for uncovering dust-obscured cosmic star formation and galaxy evolution over cosmic time. To test its scientific capabilities, the nearby star-forming and AGN galaxy NGC 1068 was observed. This study compares the observed DESHIMA 2.0 spectrum against published literature on NGC 1068, addressing the research question:

> *Is the wideband spectrum of NGC 1068 obtained with DESHIMA 2.0 consistent with previously published observational data?*

The dust continuum was extracted by fitting a grey-body with a statistical model using a Markov Chain Monte Carlo (MCMC) sampler over the 250-280 GHz window. The best-fit parameters were found to agree with values obtained by Z-spec at the 1σ level, with a reduced $\chi^2 = 1.37$ achieved with the data and $\chi^2 = 3.32$ with continuum model over Z-spec observed data, showing good continuum recovery.

Voigt profiles were fitted to the CO(2-1) and CO(3-2) lines using single fits on continuum-subtracted spectra. The emission line fluxes comparable to those obtained with the James Clerk Maxwell Telescope (JCMT) by Qiu et al. were measured by DESHIMA 2.0, agreeing within 6–12%. However, significant differences were observed in line widths and main beam temperatures, attributed to instrumental effects such as beam dilution and smearing, as well as methodological differences between single Voigt profile and multi-component Gaussian fitting approaches.

It is demonstrated that DESHIMA 2.0 delivers reliable broadband continuum and integrated emission line fluxes consistent with other instruments for NGC 1068, validating its utility for spectral surveys of bright dusty star-forming galaxies. The observed differences in line widths and channel-to-channel calibration highlight opportunities for improved MKID correspondence and noise reduction to enable the detection of fainter emission lines in future observations.

Contents

1 Introduction

1.1. Dusty Star-forming Galaxies and Their Importance

Luminous Infrared Galaxies (LIRGs) were first discovered in the late 1990s and are known to be among the brightest galaxies in the Universe [26]. They dominate the far-infrared/sub-millimetre sky at high redshift [5]. Yet, they are almost invisible in optical/X-ray because dust absorbs the high-energy radiation and re-emits it in the sub-millimetre. Investigating their basic properties, like dust continuum and bright molecular lines, provides important information about the early star-forming Universe [3, 1]. These star-forming regions produce hundreds to thousands of solar masses of stars each year (10^2 — 10^3 $M_\odot$ yr^{-1}) [26, 12]. Observing the high-redshift properties of these star-forming galaxies can be achieved through various spectroscopic techniques. However, to efficiently characterize these distant galaxies and capture multiple redshifted lines simultaneously, ultra-wideband spectrometers are needed. For this reason, integrated superconducting spectrometers (ISS) have been developed. These ISSs enable ultra-wideband and medium-resolution spectroscopy by its on-chip filter bank and microwave kinetic inductance detectors (MKIDs) for spectral coverage. While some spectrometers may offer better spectral resolution, the ISS approach, especially for high-redshift LIRGs, creates coverage over a broad range of frequencies in a single observation. An ISS specifically designed for the detection and identification of these high-redshift ($3.3 < z < 7.6$) LIRGs is the Deep Spectroscopic High-redshift Mapper (DESHIMA) [8]. DESHIMA stands out due to its wide field of view and extensive bandwidth, which contribute to its effectiveness in capturing more redshifted spectral lines.

1.2. DESHIMA

The first generation of DESHIMA (DESHIMA 1) is a single-pixel spectrometer that covers the 332-377 GHz band with 49 spectral channels offering a spectral resolution $R \approx 380$ [8]. This first light experiment of the single pixel spectrometer was performed in October 2017 and managed to detect some astronomical targets, for instance, a redshifted CO(J = 3−2) line of VV 114, a luminous infrared galaxy at the redshift of 0.020 [8]. This success led to the development of the second version of DESHIMA: DESHIMA 2.0.

DESHIMA 2.0 is a single-pixel ISS designed to simultaneously capture a frequency range from 220 to 440 GHz across 347 spectral channels. It achieves a resolving power $R = F/\Delta F \approx 500$, here F is the centre frequency of a spectral channel and ΔF is the width of that spectral channel. Data acquisition uses DESHIMA 2.0's filterbank readout system [23], where individual Microwave Kinetic Inductance Detectors (MKIDs) monitor each spectral channel at the same time. For its observations, DESHIMA 2.0 was specifically designed to be mounted on the 10m Atacama Submillimetre Telescope Experiment (ASTE). ASTE is a Telescope in the Atacama Desert in Chile at an altitude of 4860 meters. This high altitude creates an arid climate and is one of the driest places on Earth [2]. These rigorous conditions make it one of the best places on earth for far-infrared spectroscopy because water vapour absorbs this kind of radiation, making ASTE a well located telescope.

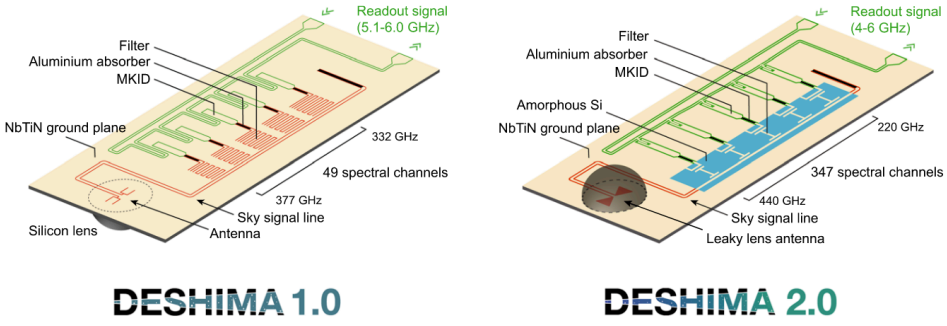

Figure 1.1: A comparison of the designs for DESHIMA 1.0 (left) and DESHIMA 2.0 (right). DESHIMA 1.0 features 49 spectral channels, while DESHIMA 2.0 showcases a design with 347 spectral channels and wider frequency coverage (220-440 GHz vs. 332-377 GHz)

Before a spectrometer can make real astronomical discoveries, it must be verified by comparing its measurements with high-quality reference data from a well-studied galaxy. An excellent example of such a galaxy is NGC 1068, a well-studied, highly luminous, and proximal galaxy [27]. Therefore, the verification process for DESHIMA 2.0 in this thesis is guided by the following research question:

> *Is the wideband spectrum of NGC 1068 obtained with DESHIMA 2.0 consistent with previously published observational data?*

To address this question, the verification process is decomposed into three objectives:

1. **Continuum extraction** Model the continuum emission from dust in NGC 1068 and subtract it from the entire wideband spectrum.
2. **Line-flux measurement** Detect and characterize bright molecular transitions, focussing on ^{12}CO(3–2) and ^{12}CO(2–1), by fitting spectral profiles to the continuum-subtracted data.
3. **Comparison** Compare the derived continuum parameters and line fluxes with the literature values for NGC1068.

1.2.1. Commissioning and Science-Verification Observations

DESHIMA 2.0 was used during a special Commissioning and Science Verification (CSV) campaign on the 10-m ASTE telescope from September 2023 to December 2024. During observation runs, the instrument recorded several astronomical sources. For the verification phase in this study, one target was chosen to provide a strong, well-studied reference. The resulting 220–440 GHz data set serves as the foundation for the continuum modelling, line-flux analysis, and comparison mentioned earlier.

1.3. NGC 1068 as a Benchmark Galaxy

NGC 1068 (shown in figure 1.2) is one of the closest LIRGs (approximately 78 Mpc) and one of the best-studied examples of a luminous Seyfert 2 galaxy that also contains an intense starburst (SB) ring in its central $\approx$ 2.5 kpc [20]. The galaxy, therefore, offers an excellent opportunity to investigate the complex relationship between star formation and AGN activity in dusty environments [14, 24].
NGC 1068 is characterized by two primary regions that DESHIMA 2.0 captured and investigated:

1. A large star-burst (SB) ring, approximately 30 arcseconds in diameter, rich in molecular clouds and active star formation. This large SB ring emits a significant part of the continuum, with its dust having a temperature of approximately 34 K, at which it emits continuum radiation. Its emissivity ϵ is less than 1, indicating it is not a perfect blackbody [27]. The density of these continuum-emitting regions is detailed in Figure 1.3.
2. A compact circumnuclear disk (CND), about 312 pc in diameter, surrounding the AGN and responsible for feeding it with dense molecular gas. This CND also powers a prominent radio jet directed toward the northeast [25, 16]. The compact CND, on the other hand, is responsible mainly for

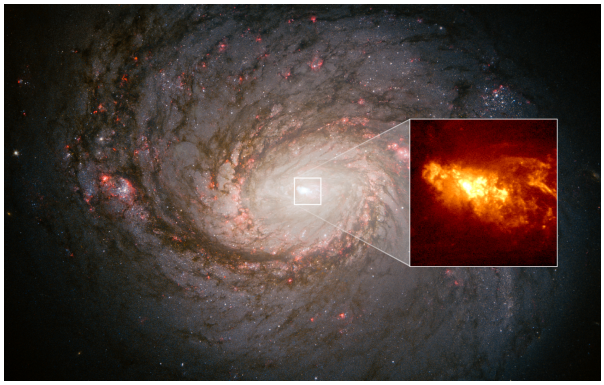

Figure 1.2: Image of NGC 1068 captured by the Hubble Space Telescope, the inset are hydrogen clouds as small as 10 light-years across within 150 light-years of the core.[18].

the prominent emission line features, as evidenced by the brightness scale distributions for both CO(2-1) and CO(3-2) shown in Figure 1.4.

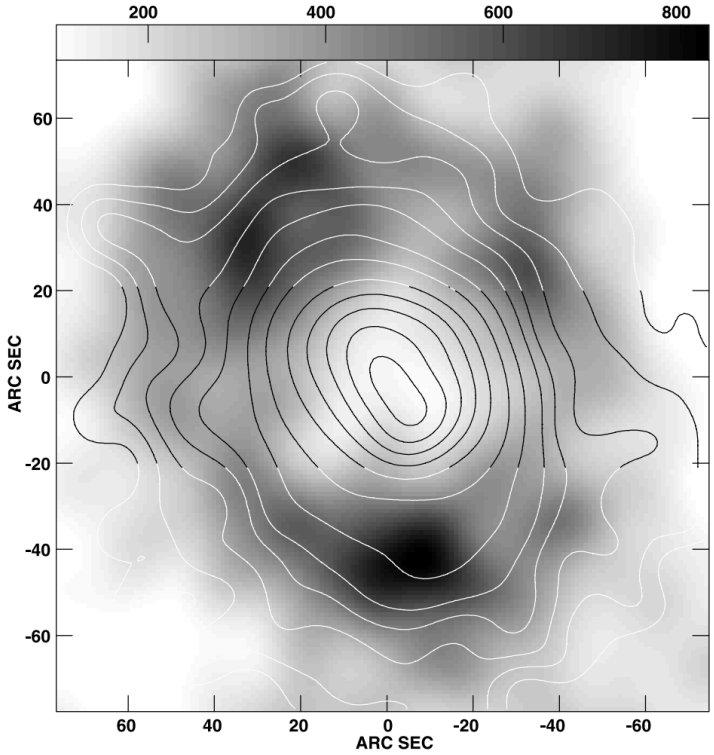

Figure 1.3: Continuum emission density of NGC 1068 [20]. The image displays velocity-integrated H I brightness in grayscale, with contours showing 850 μm (top) and 450 μm (bottom) continuum emission.

The galaxy's continuum and emission line properties, combined with its proximity, make it an ideal calibration source for testing and validating the DESHIMA 2.0 instrument.

Structure of this Thesis

First, the methodology for validating the DESHIMA 2.0 instrument will be explained in Chapter 2. This will be followed by elaborating on the values and models obtained through the methodology in Chapter 3. In Chapter 4, these results will be discussed and explained through physical interpretations. Finally, in Chapter 5, the key findings will be summarized, and we will provide recommendations for future improvements and observational strategies.

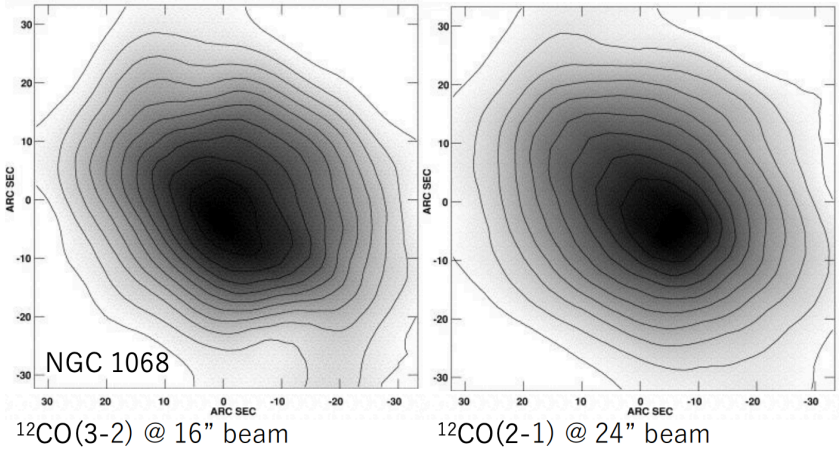

Figure 1.4: Density of CO(3-2) (left) and CO(2-1) (right) emission in NGC 1068. The left panel shows CO emission from the J=3−2 transition at a resolution of 16” with a grayscale range of 0.060–0.456 K. The right panel shows CO emission from the J=2−1 transition at a resolution of 24” with a grayscale range of 0.075–0.535 K. The velocity interval for both maps is Δv=950–1300 km s^{-1}.

2

Methods

In this chapter, we discuss the methods used to analyze and compare the DESHIMA 2.0 data collected at ASTE during the CSV campaign in 2023. We begin by detailing the attachment of DESHIMA 2.0 to ASTE for data acquisition relevant to this thesis. Following this, we describe the observational campaign and the subsequent data processing. Next, we outline the Markov Chain Monte Carlo (MCMC) methods and Bayesian statistics used for continuum fitting, which form the foundation for obtaining model parameters. Once the continuum fitting is completed and the relevant parameters are obtained, the processed data will be adjusted by subtracting the MCMC fitted continuum. This allows us to derive the parameters associated with the emission lines. Ultimately, this chapter establishes the necessary groundwork for comparing our observational analysis results with those previously reported by Kamenetzky et al. [15] and Qiu et al. [22].

2.1. DESHIMA 2.0 on ASTE system overview

DESHIMA 2.0 was deployed on the ASTE telescope in 2023 for the observational campaign. As mentioned, DESHIMA 2.0 was initially designed for the 220-440 GHz range. However, in the fabrication process this changed to a 200-400 GHz range.

2.1.1. DESHIMA 2.0 on ASTE System Setup

Beyond the characteristics of DESHIMA 2.0 explained in Section 1.2, the overall setup, including DESHIMA 2.0 attached to ASTE, played a crucial role in the data acquisition process. DESHIMA 2.0 is equipped with a two-beam setup, which allows for rapid switching between the sky (atmosphere) and an astronomical source. This two-beam setup is further explained in Subsection 2.1.2. A chopper, shown in Figure 2.1, was used to switch between these two beams. The primary objective of this switching is to filter out atmospheric fluctuation.

Finally, to function as superconductors, the MKIDs require extremely low temperatures, which is achieved using a cryostat. For this the DESHIMA 2.0 system is cooled to around 120 mK. This temperature creates a state in which the MKIDs work as superconductors in the photon-noise limit [7].

2.1.2. Data Acquisition and Initial Processing

During data acquisition, ON-OFF position switching, also called beam-switching, was used. This technique involves quickly alternating between observing the astronomical source and a ”blank” area of the sky. By looking at the blank sky area, the atmospheric fluctuations contributing to irrelevant observational data can be isolated.

For effective beam-switching, the two beam positions need to be far enough apart to avoid contamination of the ”blank” region data by the source. In this study, the two beams were positioned 233.6 arcseconds apart and alternated between beams at a frequency of 10 Hz [21]. Since the maximum beam size is at the lowest frequency and is about 30 arcseconds [17], this separation ensures that there is no overlap between the two beam positions in the sky, as the distance is more than seven times the beam size.

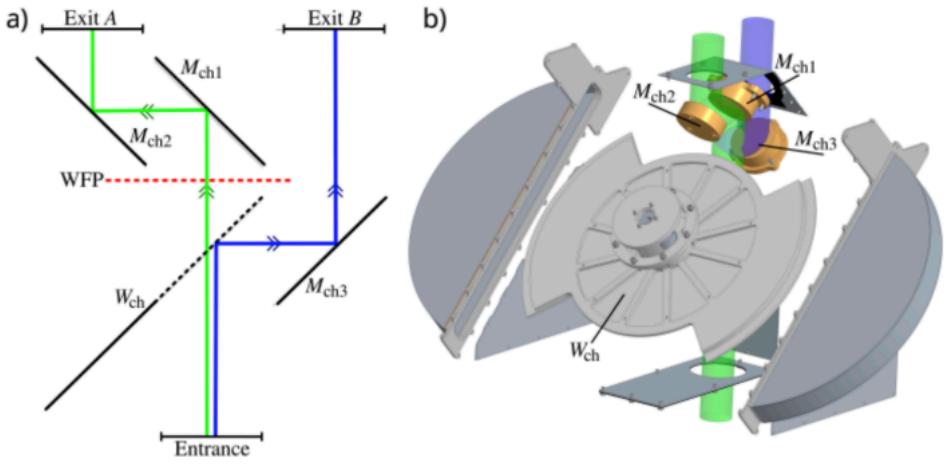

Figure 2.1: Schematic and 3D rendering of the DESHIMA 2.0 chopper system. a) The optical path shows how the chopper (Wch) switches between two exits, Exit A and Exit B, using mirrors (Mch1, Mch2, Mch3) for beam switching. b) A 3D rendering of the chopper mechanism within the DESHIMA 2.0 system.

The specific method used for beam-switching was the ABBA-chopping technique, which helped obtain a spectrum with the atmospheric noise filtered out as much as possible. A detailed analysis of the ABBA-chopping technique is outside the scope of this report but can be found in [21].

ON-OFF chopping effectively minimizes the impact of atmospheric fluctuations. However, slower and static offsets, for instance, can still be present. To account for these, a technique known as ”nodding” is used. Nodding means moving the entire telescope dish periodically to switch between two slightly different sky positions. This helps subtract any leftover background signals that remain after chopping.

2.1.3. From Gathered Data to Antenna Temperature T_A^*

The incoming signal is measured as a resonance shift of the MKID in our readout system. Through skydip calibrations this resonance frequency shift of a MKID is converted to line-of-sight brightness temperature of the sky T_{sky} using a setup based on the model in the report of Takekoshi [28]. This sky temperature can change based on atmospheric conditions like precipitable water vapor (PWV), wind, and the elevation of the telescope (which can vary between . This sky temperature is defined as [7]:

$$T_{sky} = (1 - \eta_{atm}) T_{sky,physical} \tag{2.1}$$

In this equation, $T_{\text{sky,physical}}$ is about 270 K and η_{atm} is the atmospheric transmission factor. Observations by Peters [21], shown in Figure 2.2, reveal peaks in the plot around 325 GHz and after 360 GHz.

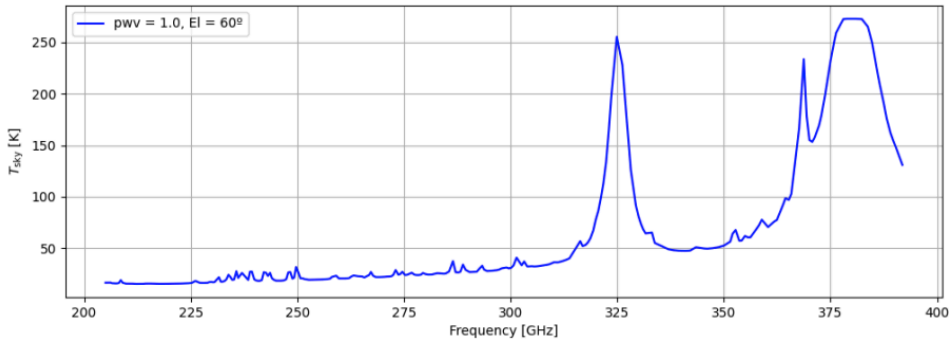

Figure 2.2: T_{sky} against frequency for each channel corresponding to a frequency band using equation 2.1. This figure was created in the report of Peters [21].

These peaks indicate very low atmospheric transmission, as they correspond to water vapor ab-

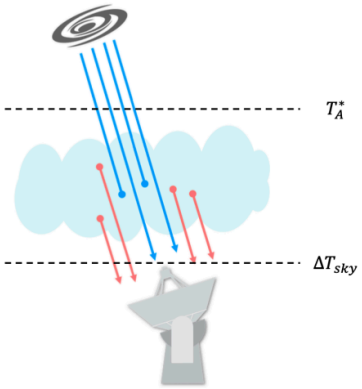

Figure 2.3: Diagram illustrating the relationship between the observed antenna temperature (T_A^*) and the change in sky temperature (ΔT_{sky}) due to an astronomical source observed through the atmosphere

sorption lines. In these regions, which then re-emit this energy as their own thermal radiation. This makes the atmosphere appear very bright, which introduces additional noise into observations within these frequency regions. The peaks suggests that $\eta_{atm} \approx 0$, which implies $T_{sky} \approx T_{sky,physical}$. This is important since this explains the increased noise for the given regions in figure 2.4.

The data, initially expressed as T_{sky}, was processed using the beam-switching technique. This produced ΔT_{sky}, which represents the sky temperature after chopping. The final data product used in this thesis is the atmosphere-corrected antenna temperature, T_A^*. It is related to ΔT_{sky} by the equation $T_A^* = \frac{\Delta T_{sky}}{\eta_{atm}}$. In Figure 2.3, we can clearly see the average spectrum of atmosphere-corrected antenna temperature in relation to the sky temperature.

2.1.4. Observation runs on ASTE

While DESHIMA 2.0 was installed to the ASTE telescope, it obtained several observations of NGC 1068. For this research, five distinct on-sky observations of the galaxy were utilized. These observations were taken on consecutive days: September 19, 20, 21, 22, and 23, 2023. All observations were conducted between 8:00 and 10:00 UTC. The spectra obtained by the observation runs are shown in figure 2.4 (All individual spectra are shown in figure C.1).

2.2. Data Reduction Pipeline

The on-sky observations of NGC 1068, conducted with DESHIMA 2.0 during the September 2023 ASTE observation runs, provided data that needed processing to get reliable results. These measurements captured useful information, but also included outliers and missing data in some channels. This could affect the reliability of the results. A data reduction pipeline was created to transform these initial noisy observations into a new dataset. The process involved two main steps: sigma-clipping to remove outliers and spectra stacking to combine multiple observation runs and achieve full spectral coverage over the frequency range obtained by DESHIMA 2.0.

2.2.1. Sigma-Clipping: Outlier Mitigation

Sigma-clipping is a method used to remove outliers from a dataset [30]. This technique is used for reducing data, where peaks in noise caused by instrumental interference lead to significant deviations in its data. The method first calculates the mean and standard deviation of data and then removes repeatedly data points that fall outside a specific multiple of the standard deviation from the mean.

In this study, we used sigma-clipping on the frequency-domain spectral data. For each of the five observation runs, we applied sigma-clipping to the flux uncertainty values of individual spectral channels. This process eliminated channels, for the spectra of each observation run apart, where the measurement uncertainty was an outlier. As a result, we improved the data quality. We used the $astropy.stats.sigmaclip$ function with a 3 σ clipping factor and a maximum of 5 iterations. The 3σ

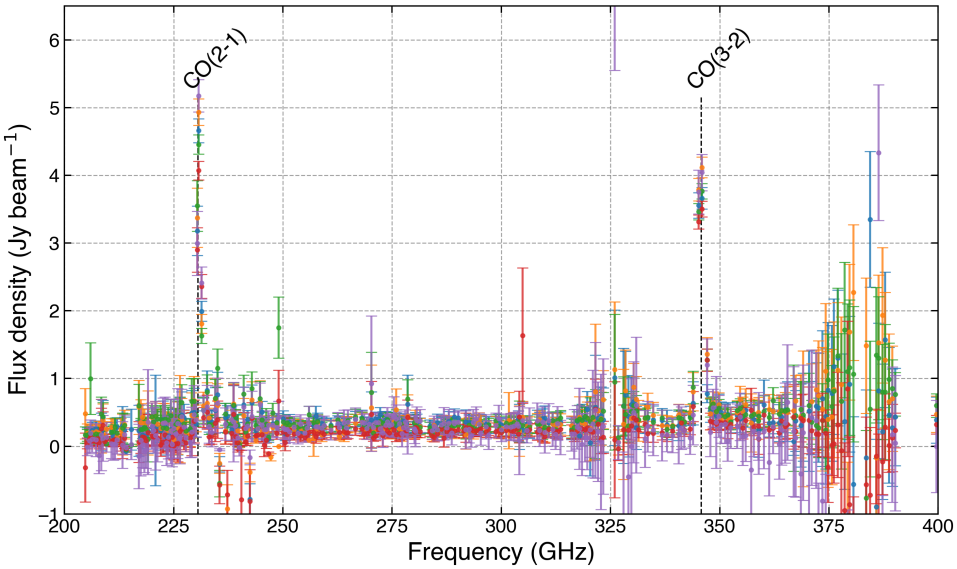

Figure 2.4: This figure displays the observed flux density in (Jy/beam) as a function of frequency in (GHz). The data shown is are the spectra obtained by the individual observation runs. Each run has its own colour for distinction. Error bars represent the 1-sigma uncertainty on each individual flux measurement.

clipping factor refers to the method of removing data points that are more than three standard deviations from the mean. This process took place for a maximum of 5 iterations. During each iteration, the mean and standard deviation were recalculated, and outliers were removed. This continued up to five times or until there were no more outliers within the 3σ limit. This approach helped us obtain more reliable data before further processing. The impact of this sigma-clipping on the data is shown in Figure 3.1, where the removed data points are highlighted in red.

2.2.2. Data Stacking: Enhancing Signal-to-Noise and Completeness

Even with sigma-clipping, individual observation runs can have data gaps that hinder fitting. To address this, we stacked five observation runs. This process improved the signal to noise ratio (SNR).

Stacking involved precisely aligning and summing data from each observation run, performed step-by-step for each spectral channel. This primarily increased the overall SNR by averaging out random noise components through a weighted average, where the weights used were the inverse of the individual observation's variance ($1/\sigma_i^2$) for that specific spectral channel. As demonstrated in Figure 2.5, the noise was significantly reduced with the increasing number of stacked spectra. This confirmed the effectiveness of our stacking approach in improving the SNR per channel. The relationship between the standard deviation (σ) and the on source time in seconds is quantitatively described by the following equation:

$$\sigma \propto t^{-0.56\pm0.04} \tag{2.2}$$

This relationship found by stacking shows that for each extra spectra observation of a certain period the standard deviation scales with a factor $t^{-0.56}$, showing the efficiency of stacking. After stacking, a mask based on a Signal-to-Noise Ratio (SNR) of at least three was applied to the data, ensuring a robust data basis for further analysis shown in figure 3.2.

2.2.3. Converting parameters for comparison

For the comparison to the literature, the observed parameters need to be in the same units as those in the compared literature. However, the initial data obtained from DESHIMA 2.0 for this thesis were in different units as the parameters used in the paper of Kamenetzky et al. [15] and Qiu et al. [22]. The data obtained from the observation runs of DESHIMA 2.0 are in units of Kelvin. To convert these measurements into flux density (F_ν) in Jansky per beam (Jy/beam), the following conversion factor

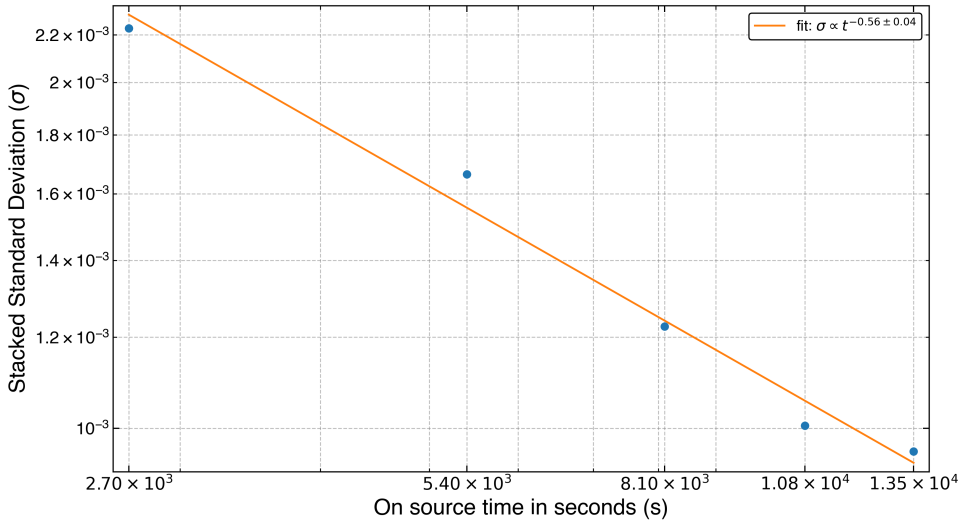

Figure 2.5: Comparison of Signal-to-Noise Ratio (SNR) before and after stacking. This figure illustrates the reduction in noise and therefore consequent increase in SNR per channel achieved by coherently stacking the multiple observations of NGC 1068. With on the y-axis the variance of the data points and on the x-axis the on source time (each observation had the same 45 minute length). The stacking was done over channel 170 (corresponding to channel with centre frequency of 230.72 GHz) which had values for the flux density for every observation

based on the telescope's effective aperture was applied. The brightness temperature and flux density values were calculated for each data point.

The conversion utilizes the Rayleigh-Jeans approximation, valid for the observed frequencies, and is given by:

$$F_\nu = \frac{2k_B T_A}{A_e}$$

where the flux density F_ν is typically expressed in W/m^2/Hz. To convert this to Jansky, a factor of 10^{26} is applied, as 1 Jy $= 10^{-26}$ W/m^2/Hz. Thus, the final equation for conversion used is:

$$F_\nu \text{ (Jy/beam)} = \left(\frac{2k_B T_A}{A_e}\right) \times 10^{26}$$

The variance corresponding to the flux density (F_{sig}) is converted similarly to the equations above.

2.3. Continuum Fitting: Problem Definition and Model Selection

To get a robust conclusion to the research question both the continuum and the emission lines need to be analysed and compared to literature. However, the continuum also provides a challenge for the observation of the emission lines as it forms a baseline flux, which rises with the frequency, as shown in figure 2.6. Therefore, it is essential to subtract this continuum before analysing the emission line features. Fortunately, galaxy NGC 1068 is well-studied with a reliable continuum model. Kamenetzky et al. (2011) characterised this continuum through observations with the Z-spec instrument at the Caltech Submillimeter Observatory (CSO) [19] [15]. The approximated continuum out of measurements with Z-spec is given in the following equation:

$$F_\nu = A\left(\frac{\nu}{240\text{ GHz}}\right)^{B-2} \Omega B_\nu(T)\left(1 - e^{-(\nu/\nu_0)^\beta}\right) + F_{0,\text{core+jet}}\left(\frac{\nu}{230\text{ GHz}}\right)^{-\alpha} \text{Jy.} \tag{2.3}$$

The continuum fit, F_ν, is represented by two terms: a beam-scaled graybody and a power-law component from the core and jet. The first term describes the beam-scaled graybody. Here, A, B, α, and β were treated as free parameters for the fit. The other parameters were held fixed, with Ω being the source size (e.g., 1.66×10^{-8} sr for a 30" ring), $B_\nu(T)$ being a blackbody of dust temperature $T = 34$ K, $\nu_0 = 3000$ GHz characterizing the dust emissivity, and $F_{0,\text{core+jet}} = 0.028$ Jy representing the measured flux density at 230 GHz. All these fixed parameters (Ω, T, ν_0, $F_{0,\text{core+jet}}$) were adopted directly from

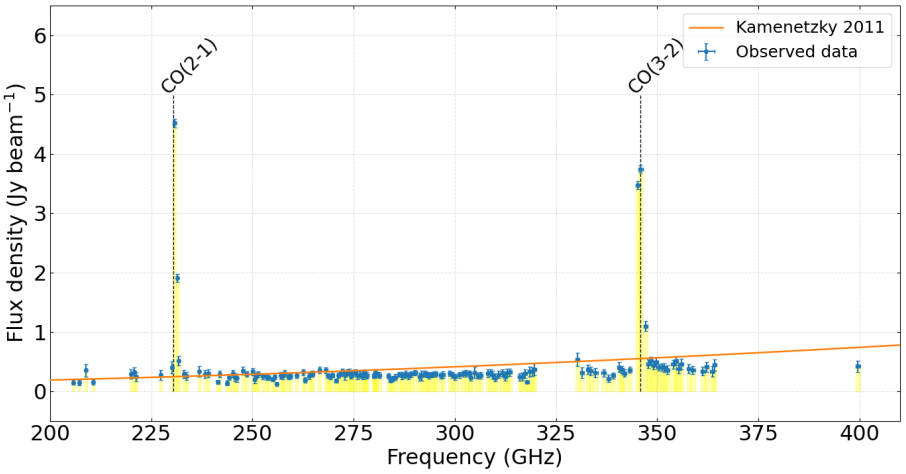

Figure 2.6: Stacked spectrum, derived from five different sigma-clipped spectra. The horizontal axis shows frequency in GHz. The vertical axis indicates flux density in Jy beam^{-1}. The yellow rectangular areas illustrate the spectral coverage of each channel. The solid orange line represents the continuum according to the Kamenetzky (2011) model. Two prominent emission features, labeled as CO(2-1) and CO(3-2) transitions, are clearly visible.

Kamenetzky et al. [15]. The second term, $F_{0,\text{core+jet}} \left(\frac{\nu}{230\ \text{GHz}}\right)^{-\alpha}$ Jy, accounts for the core and jet contribution. The SB ring dominates the continuum of Kamenetzky, this is the first part of the equation, but a small contribution ($\approx 10\%$) is also present from the central disk and the jet of the Active Galactic Nucleus (AGN), which is present by the $F_{0,\text{core+jet}}$ part of the equation. Following this continuum model, a fitting can be done on the data of DESHIMA 2.0.

2.4. Bayesian Framework for Spectral Analysis

Now that we have put together a framework for the continuum fitting, we need a statistical method that will estimate the continuum parameters with the highest likelihood. Using a statistical method provides a robust way of minimizing the uncertainties and finding an interval in which the parameters are most likely to be found. Bayesian statistics provide a good framework by integrating prior knowledge and quantifying the degree of conviction in hypotheses based on observed evidence. This approach was used in finding parameters based on the data observed by DESHIMA 2.0.

2.4.1. Bayesian statistics

Bayesian statistics offers a powerful approach by incorporating prior beliefs about a hypothesis and subsequently updating these beliefs based on observed evidence, and with that quantifying our degree of conviction. Bayesian statistics are based on Bayes theorem:

$$P(H|E) = \frac{P(E|H) \times P(H)}{P(E)} \tag{2.4}$$

In this fundamental equation:

- $P(H|E)$ represents the **posterior probability**: the probability that the hypothesis (H) is true given the observed evidence (E). This is our updated belief after considering the data.
- $P(E|H)$ is the **likelihood**: the probability of observing the evidence (E) if the hypothesis (H) were true. It quantifies how well the hypothesis explains the observed data.
- $P(H)$ is the **prior probability**: the initial probability assigned to the hypothesis (H) being true, before any evidence is considered. This reflects our pre-existing knowledge or assumptions.
- $P(E)$ is the **marginal likelihood** or **evidence**: the total probability of observing the evidence (E) across all possible hypotheses. It acts as a normalizing constant.

The advantage of Bayesian statistics lies in its ability to incorporate prior information ($P(H)$) and then, through the likelihood function ($P(E|H)$), systematically update this prior to form a robust posterior probability ($P(H|E)$). This iterative process of updating beliefs based on evidence is why Bayesian statistics is well-suited for the analysis of the continuum model.

2.4.2. Prior selection

In the Bayesian framework, prior probabilities are essential for forming posterior probabilities. These prior beliefs constitute the initial knowledge for estimating the continuum model parameters before incorporating the DESHIMA 2.0 observation data. For this study, Gaussian prior distributions were selected for all four free parameters (A, B, α, β) of the continuum model. As Kamenetzky measured with a similar type of spectrometer and a similar type of Telescope (the CSO), it is reasonable to adopt the posterior distributions found by Kamenetzky as the prior distributions for the data exploration. This approach ensures that the priors have a comprehensive parameter range without imposing strict restrictions. The prior specifications are detailed in Table 2.1.

Table 2.1: Prior distributions used for the MCMC continuum fitting.

Parameter	Prior Type	Mean (μ)	Std. Dev. (σ)
A	Gaussian	0.0446	±0.01
B	Gaussian	0.421	±0.27
α	Gaussian	0.9	±0.2
β	Gaussian	2.0	±0.5

2.4.3. Likelihood formulation

The likelihood function, $P(E|H)$, quantifies the probability of observing the DESHIMA 2.0 spectral data (E) given a set of continuum model parameters (H). For a given set of model parameters, the likelihood was formulated assuming normally distributed residuals between the observed flux density and the model's predicted observed flux density, weighted by the observational uncertainties. Specifically, a Gaussian likelihood function was used, where the observed data points (f_i) were compared against the continuum model (m_i) as defined in Equation 2.2. For this model the likelihood is given by:

$$L(\theta) = \prod_{i=1}^{N} \frac{1}{\sqrt{2\pi\sigma_i^2}} \exp\left(-\frac{(f_i - m_i)^2}{2\sigma_i^2}\right) \quad (2.4) \tag{2.5}$$

where $L(\theta)$ represents the likelihood for the parameter set θ, summed over N observed data points, with σ_i^2 being the variance of each observed data point.

2.4.4. Forming Posteriors

Combining our Gaussian priors (Table 2.1) with the likelihood defined in Equation 2.5 via Bayes' theorem (Equation 2.4) yields the joint posterior distribution for the continuum parameters $\{A, B, \alpha, \beta\}$. However, the multi-dimensional integral required to normalize this distribution cannot be evaluated analytically. To overcome this, we approximate the posterior by drawing a large ensemble of parameter samples using Markov Chain Monte Carlo (MCMC) explained in the next section 2.5.

2.5. MCMC method and implementation

To sample the high dimensional posterior introduced above, we implement a Markov Chain Monte Carlo (MCMC) algorithm. MCMC is particularly well suited for Bayesian inference when multiple, potentially correlated parameters must be estimated simultaneously, since it builds up the posterior distribution through repeated sampling rather than analytic integration. Specifically, we use the Metropolis-Hastings algorithm [13]. This iteration of MCMC proposes new states based on a proposal distribution. Then, it accepts or rejects these states based on likelihood.

The MCMC approach relies on two key ideas:

- **Monte Carlo sampling**: Random proposals are drawn to explore the parameter space, accumulating a numerical representation of the target distribution.

- **Markov chain**: Each proposed sample depends only on the current state, so after an initial burn-in period the chain converges to the true posterior. The burn-in period refers to the first iterations of the chain that are removed afterwards. These iterations are affected by the starting values (priors) and do not represent the target distribution yet.

At each iteration, the sampler proposes a new set of parameters and computes the ratio of posterior probabilities between the trial and the current point. The trial is then accepted or rejected with a probability equal to this ratio. Once the burn in phase is discarded, the remaining samples form a faithful ensemble of the posterior, from which we extract best fit values and credible intervals.

2.5.1. Software choice

For the MCMC method, the emcee module [9] in Python was used. The emcee module makes use of an affine-invariant ensemble sampler. This algorithm is an advanced variant of the Metropolis-Hastings algorithm. It operates with an ensemble of ”walkers,” where each walker’s proposal for a new position is informed by the current positions of other walkers within the ensemble [11]. This approach creates a way of effectively and efficiently exploring multiple parameters that can be correlated, which increases the convergence speed and reliability for multiple parameter models. Making it a more suiteed approach than traditional single-chain methods.

2.5.2. Computational setup

Several parameters should be configured to start the MCMC sampling process with the emcee module. Increasing these parameters, like the number of walkers, usually results in a more accurate and reliable estimate of the model parameters. To define the spectral region for characterizing the continuum, the initial MCMC fitting was done on data within the range of 250 GHz to 300 GHz. This specific range was selected because it is expected to be free from atmospheric absorption features and molecular emission lines, ensuring the continuum is as pure as possible for effective modelling. The particular setup for the MCMC algorithm used in this application is outlined in Table 2.2.

Table 2.2: Relevant Specifications of the MCMC method for continuum fitting.

Parameter	Value
Number of walkers	32
Number of steps	2×10^6
Burn-in Period	2×10^4

2.6. Line Fitting

After the continuum is removed from the stacked spectra obtained in the figure 2.6 the line fitting procedure can be performed. The molecular emission lines are affected by both astrophysical and instrumental broadening effects. While Doppler motions within galaxies broaden emission line profiles into Gaussian shapes [4], DESHIMA 2.0’s finite spectral resolution introduces additional instrumental broadening that can be seen as a Lorentzian response, causing incoming signals to spread across multiple channels [29]. These broadening mechanisms show the need for an approach to line fitting that can disentangle these effects and extract the physical parameters needed for comparison. These physical parameters include the line width, peak main beam temperature and flux density.

For this, a line fitting procedure was formed that accounts for both broadening mechanisms. The approach begins by subtracting the fitted continuum model (as demonstrated in Figure 2.6) from the observed spectrum to isolate the emission line features, resulting in the residual spectrum. This residual spectrum, which already includes the instrumental broadening from the DESHIMA channel response, is then modelled.

The core of our fitting method uses Voigt profiles. These profiles naturally include a convolution of a Lorentzian with a Gaussian, representing independent broadening mechanisms. In our model, the Voigt profile combines the instrumental broadening from the DESHIMA channel (Lorentzian) response

with the intrinsic astrophysical line shape (Gaussian). The Voigt model is expressed as:

$$V(x;\gamma,\sigma) = (L * G)(x) = \int_{-\infty}^{\infty} L(x - x';\gamma)G(x';\sigma)dx' \tag{2.6}$$

where x represents the frequency, ν_0 is the center frequency, σ represents the width of the Gaussian component, and γ is the half-width at half-maximum (HWHM) for the Lorentzian component. Importantly, the Lorentzian HWHM, γ, is determined by the center frequency ν_0 and the quality factor Q of the DESHIMA channel through the equation $\gamma = \frac{\nu_0}{2Q}$. We used pre-measured, frequency-dependent Q-factor values to accurately the instrumental broadening, these Q factors are also shown in figure D.1a.

Our fitting procedure follows a four-step approach to ensure reliable parameter extraction:
Data Selection and Windowing: For each target emission line, we set a frequency window centered on the expected line position based on literature values. For example, CO(2-1) is at 230.538 GHz and CO(3-2) is at 345.796 GHz. This method narrows the fitting to the relevant spectral area while trying to avoid possible interference from nearby features.

Parameter Estimation: Instead of random starting values, we get initial guesses based on the observed spectrum. The peak flux density gives us the amplitude estimate, and the apparent line width provides the initial width parameter. This approach based on data helps make convergence more reliable and lowers the chance of finding false local minima.

Weighted Optimization: We use curve fitting to minimize the weighted least-squares difference between the observed data and the Voigt model. The weighting scheme includes measurement uncertainties, or error bars, to ensure that areas with higher signal-to-noise ratios influence the fit more. This approach improves the precision of the parameters.

Parameter Derivation: After successful convergence, we change the fitted parameters into meaningful quantities. We convert the line width in GHz to km/s using the relativistic Doppler formula E.2. We also compute the line flux by integrating the fitted profile over a velocity range. This line flux is then converted from Jy·km/s to milliKelvin·km/s E.1. These derived parameters allow for direct comparison with literature values and evaluation of the instrument's scientific performance.

This fitting method helps us obtain four important parameters for each emission line: the integrated flux density, the line width (in both frequency and velocity units), the exact centre frequency, and the peak temperature. By comparing these values with results from existing literature, we can assess DESHIMA 2.0's scientific performance and confirm its ability for precise submillimeter spectroscopy.

2.7. Comparing Observational Analysis Results

With the method for continuum and line fitting procedures set, the next step is to apply these techniques to the observed data from the NGC 1068 observation runs. The main goal of this research is to compare the parameters from our analysis with those reported in the literature. We specifically compare the continuum model parameters from Kamenetzky et al. (2011) [15] and the emission line parameters from Qiu et al. (2020) [22].

Weighted Least Squares Chi-Squared (χ^2) test To compare the continuum, we use the Weighted Least Squares Chi-Squared (χ^2) statistic to measure how well the observed data matches the model predictions. In this thesis, we calculate the reduced χ^2 values for the MCMC-derived model, which uses DESHIMA 2.0 on ASTE data, and a reference model with fixed parameters from Kamenetzky's work with Z-spec on CSO. This allows us to evaluate how well each model describes the observed continuum.
The (χ^2) statistic is calculated as follows:

$$\chi^2 = \sum_{i=1}^{N} \frac{(O_i - E_i)^2}{\sigma_i^2} \tag{2.7}$$

Here, O_i represents the i^{th} observed data point, E_i is the corresponding model-predicted value, σ_i^2 is the variance of the i^{th} observed data point and N is the total number of data points.
The reduced (χ^2): (χ^2_{red}) is defined as

$$\chi^2_{red} = \frac{\chi^2}{N-k} \tag{2.8}$$

In this equation, k represents the number of free parameters. The reduced χ^2 accounts for the degrees of freedom. A χ^2_{red} value close to one indicates a good fit, meaning that the differences between the model and data align with the measurement uncertainties. However, a value larger than one shows a poor fit or a discrepancy between the two models.

The continuum model parameters from Kamenetzky et al. are listed in table 2.3. The emission line fitting parameters for the CO(2-1) and CO(3-2) transitions from Qiu et al. are shown in table 2.4. These comparisons will help evaluate the precision of DESHIMA 2.0's observational abilities and its consistency with established models in the literature.

Table 2.3: Values found for the continuum model parameters by Kamenetzky et al. [15].

Parameter	Mean (μ)	Std. Dev. (σ)
A	0.0446	± 0.01
B	0.421	± 0.27
α	0.9	± 0.2
β	2.0	± 0.5

Table 2.4: Rotational transition emission line properties from Qiu et al. [22], including multiple velocity components for Gaussian fitting of CO(2-1) from JCMT observations.

Transition	Frequency (GHz)	Flux (mK km/s)	Line width (km/s)	Main beam Temperature (mK)
CO(2-1)	**230.538**			
Component 1		203600 ± 20500	63 ± 9	313.3
Component 2		220000 ± 26000	179 ± 16	802.0
Component 3		203600 ± 20500	81 ± 10	337.4
CO(3-2)	345.796	166000 ± 20000	(-)	630

The rotational transition emission line properties for CO(2-1) in Table 2.4 include three components. Qiu et al. (2020) used three different velocity components for their Gaussian CO(2-1) emission fitting. To compare these values with what we obtain from our analysis, which uses a Voigt profile fit, we need to find the best way to bridge these different methods.

The most straightforward comparison is for the integrated flux. The individual Gaussian fits and a single Voigt profile fit show the total emission across the line. We can directly compare the fluxes from the three components reported by Qiu et al. (2020) with the integrated flux from our single Voigt profile fit. This straightforward comparison lets us accurately assess the total observed line strength.

Our single Voigt profile fit provides an overall line width describing the blended emission feature. In contrast, Qiu et al.'s analysis breaks this down into individual line widths for each of their three components. A weighted average (given in table 2.5) of these individual line widths, based on their respective fluxes, gives us a sense of the average intrinsic broadening of the gas. We expect the overall line width from our single Voigt fit to be larger than this weighted average. This is because our single Voigt profile captures not only the broadening within each gas component but also the spread caused by the different velocities and velocity structures of these multiple components across the entire line.

Table 2.5: Weighted Average Properties for CO(2-1) derived from Qiu et al. [22] components.

Transition	Parameter	Weighted Average Value
CO(2-1)	Line Width (km/s)	116.5
	Main Beam Temperature (mK)	602.8

3

Results

This chapter presents the results of the observational analysis of NGC 1068 using DESHIMA 2.0 data collected during the commissioning and science verification (CSV) campaign at ASTE. The results are organised according to the framework described in Chapter 2. They progress from data reduction through continuum fitting to emission line analysis and comparison with literature values.

3.1. Data reduction

Before the results could be analysed, the data reduction pipeline was performed on spectra obtained by the five individual observation runs (shown in figure 2.4). The data after sigma clipping had an overall average SNR across all observation runs of 2.32. However, a minimum of an SNR ratio of 3 was used to obtain the results.

3.1.1. Sigma-clipping and masking effectiveness

From the data across all five observation runs, we identified and removed outliers using a sigma clipping algorithm. This excluded approximately 26% of the data points in the frequency domain. Most of the removed points were located around 325 GHz and in the 375-400 GHz range, where atmospheric absorption is strong. After this, we applied the SNR threshold mentioned in the method section, which further filtered the data before the continuum removal step (see figure **??**). This SNR criterion resulted in an additional 27% of the points being excluded. The impact of the reduction process is shown in figure 2.6. We validated the effectiveness of the sigma-clipping process by comparing the clipped dataset against the raw data (shown in figure 3.1). The figure clearly shows that the points removed by the clipping algorithm are mainly around the frequency regions where atmospheric interference takes place, confirming the working of the concept. Similarly, we validated the SNR filtering by looking at the changes to the stacked flux density spectrum (figure 3.2). The figure shows that, by applying the SNR threshold, the points with sufficient signal quality are kept. This ensures a robust final spectrum.

3.2. Continuum fitting results

The fitting procedure for characterizing the continuum was conducted on the modified stacked spectra we obtained. As described in the methodology section, we used the MCMC method to determine the continuum parameters. This section will present the trace plots for all four free parameters. These plots will visually show the convergence and sampling efficiency of our MCMC chains. We will also display corner plots illustrating these parameters' correlations. In addition, we will directly compare our continuum model defined by the derived parameters with the continuum characterized by Kamenetzky [15]. This will help us evaluate any differences or agreements with the existing literature.

3.2.1. Chain convergence

For the MCMC run with the refined frequency range, all parameters initialized walkers with the number of steps and the burn-in period are listed in table 2.2. As can be seen in the trace plot 3.3 the parameters converged well to an estimated continuum model parameter value. The trace plots are displayed in

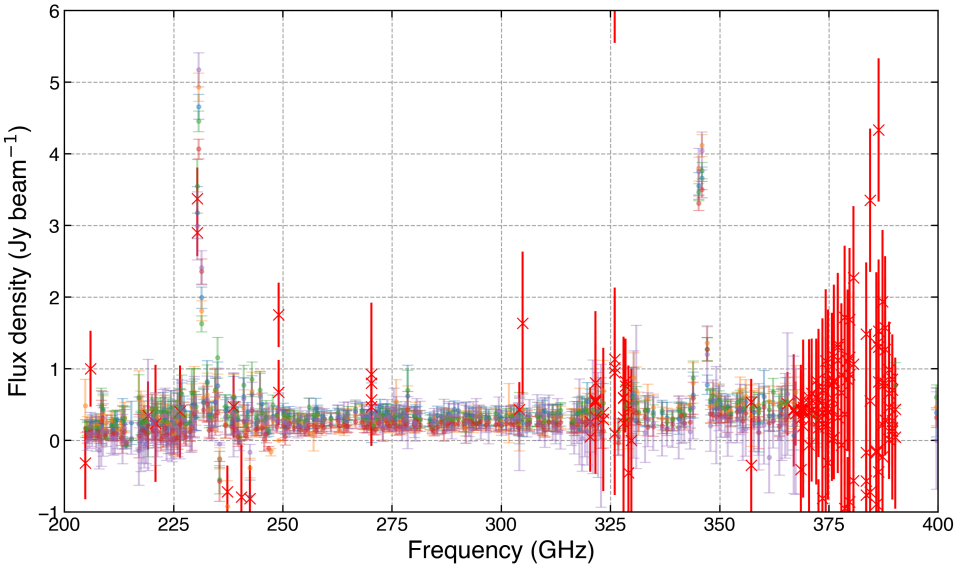

Figure 3.1: Observed flux density across frequency of the five observations all shown in different colours. Error bars represent the 1-sigma uncertainty, capped at 1 Jy for visual clarity. Outliers were removed using a 3-sigma clipping algorithm with 5 iterations on the flux density uncertainties. Points removed by the clipping are shown as small red crosses and red error bars.

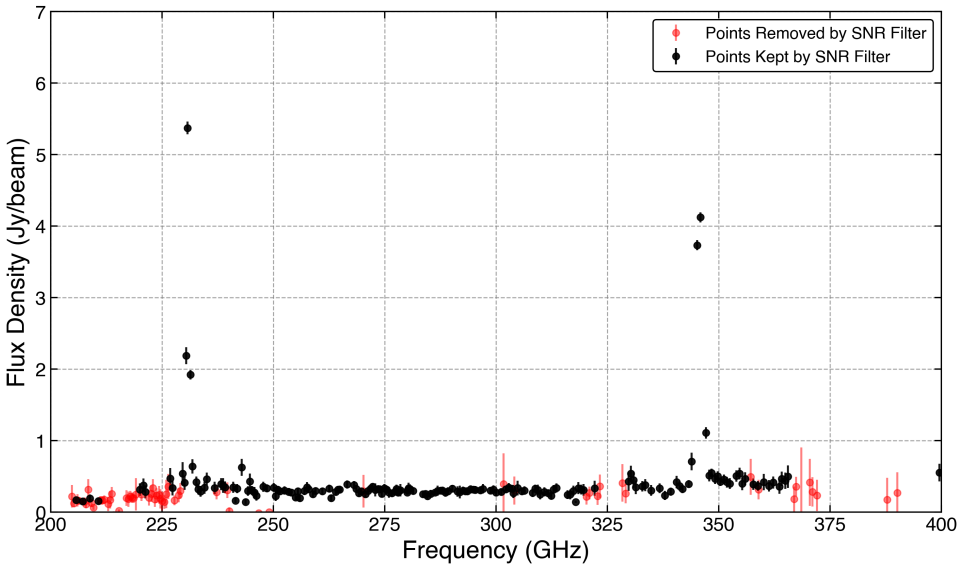

Figure 3.2: Stacked flux density spectrum showing the effect of SNR masking. Points with SNR > 3 are shown in black and kept, while points with SNR ≤ 3, which are removed from the final spectrum, are shown in red.

figure 3.3, where the burn-in of 2×10^4 steps has been applied. The trace plots show stable behaviour with no significant trends, suggesting that the chains have mixed and represent the posterior distribution for each parameter.

3.2.2. Posterior distributions

The MCMC run estimated all parameters. The numerical results of these parameters are shown in the table 3.2.

The MCMC analysis reveals varying levels of constraint across parameters. Parameter β shows the highest precision (5.2% relative uncertainty), followed by α (22% relative uncertainty) and A (25% relative uncertainty). In contrast, parameter B exhibits the largest uncertainty (242% relative uncertainty), suggesting this parameter is less well-constrained by the available data.

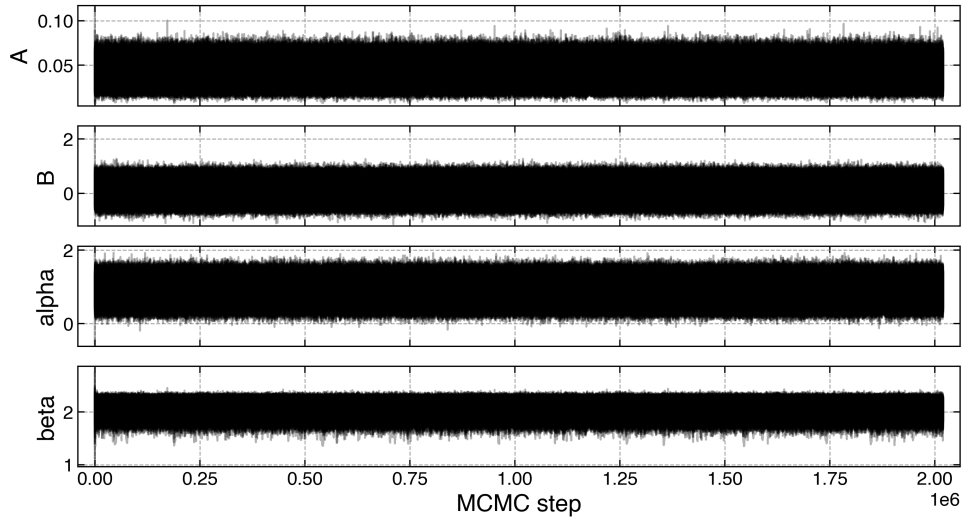

Figure 3.3: Trace plot showing how the MCMC sampler changes for the four free parameters of the continuum model (A, B, α, and β) over the 250-300 GHz range. After an initial burn-in phase, the chains mix well and show stability. This indicates that the sampler has converged to the posterior distribution.

Table 3.1: Best-fit parameters and parameter estimates for the MCMC run over the 250-300 GHz range

Parameter	Best-fit value	Uncertainty ($\pm$)
A	0.0400	$\pm$ 0.0101
B	0.0951	$\pm$ 0.2306
α	0.9121	$\pm$ 0.1985
β	2.0624	$\pm$ 0.1079

The correlation between the free parameters is shown in the corner plot 3.10. The corner plot analysis shows that most parameters do not relate to each other. However, an exception can be seen in the correlation between A and β. They have a positive correlation coefficient of approximately (Found value from the plot).

3.2.3. Continuum model fit

The continuum model, derived from the MCMC run on the 250-300 GHz frequency range can be seen in figure 3.11.
The MCMC run resulted in a model based on the Kamenetzky framework for the continuum, using the obtained posterior values. The reduced χ^2 values were calculated, giving:

- Reduced χ^2 for the MCMC best-fit model (250-300 GHz): 1.10
- Reduced χ^2 for the Kamenetzky values inserted into the model: 4.54

The MCMC model's reduced χ^2 value of 1.10 shows a good fit, meaning this model captures the data well. In contrast, the Kamenetzky model's reduced χ^2 value of 4.54 suggests it underfits the data and does not account for the observed variability effectively.

3.2.4. Refined Frequency Range Selection: 250-280 GHz

Our first continuum fit, done over the 250-300 GHz range as discussed in Section 3.2.3, showed some significant differences between our derived parameters (Table 3.1) and the established values from Kamenetzky [15] (Table 2.1), this was derived by the high reduced χ^2 values. These differences indicate the need for a more accurate method to determine the free continuum model parameters for our DESHIMA 2.0 data.

The difference between the Kamenetzky continuum model and our observed data at higher frequencies is a key observation driving this revision. As shown in Figure 2.6, the Kamenetzky model accurately

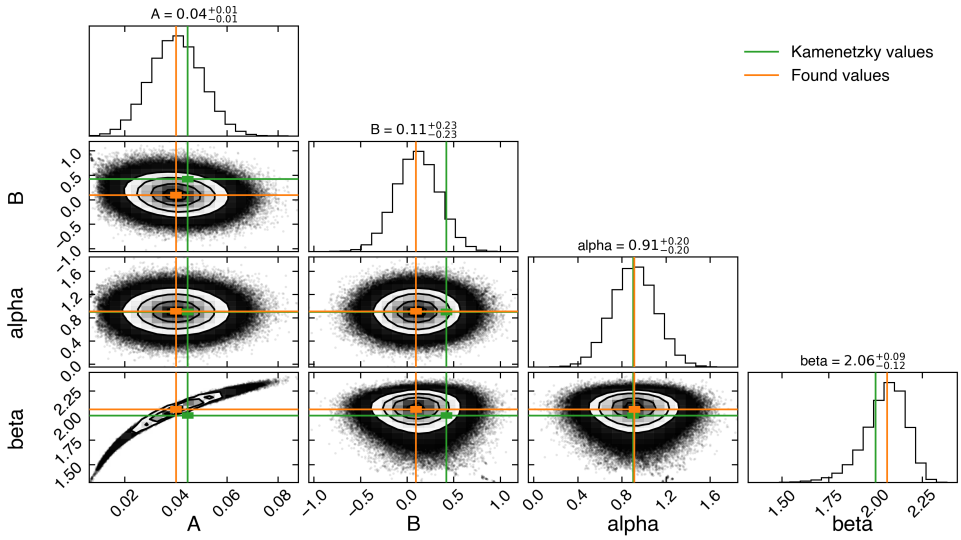

Figure 3.4: Marginalized posterior distributions for the continuum model parameters A, B, α, and β from the MCMC sampling on the 250-300 GHz range. The diagonal panels present the one-dimensional posteriors with the displayed median and 1σ uncertainties. The off-diagonal panels show the two-dimensional posterior distributions. The green lines indicate the prior (Kamenetzky) parameter values, while the orange lines represent the best-fit parameters from the MCMC run. The plot reveals possible correlations between parameters.

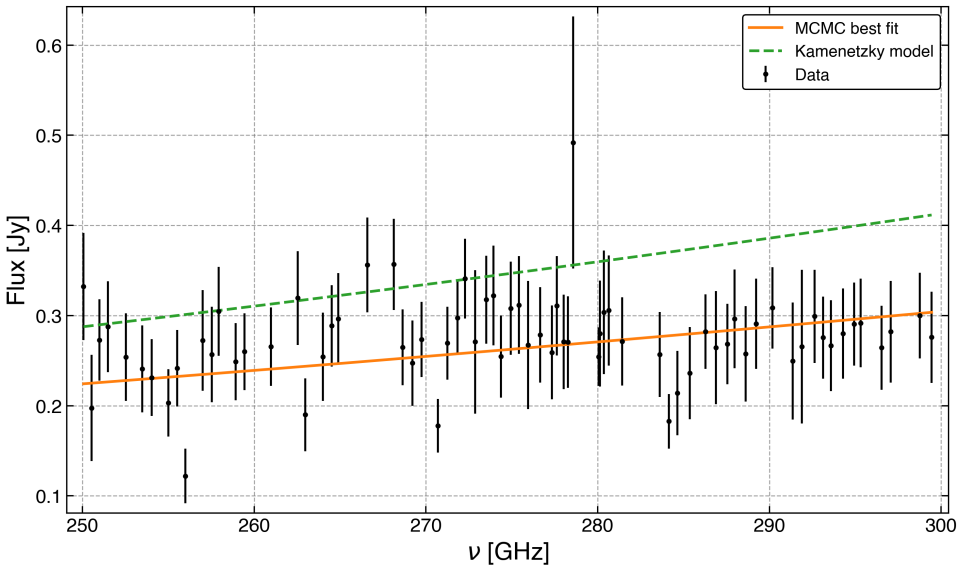

Figure 3.5: Observed flux data (black points with error bars) as a function of frequency (ν). The orange solid line represents the continuum model evaluated at the MCMC best-fit parameters for the 250-300 GHz range. The dashed green line shows the model using the initial Kamenetzky (prior) parameter values.

predicts the continuum for lower frequencies up to approximately 280 GHz. However, in the higher frequency range $>$ 280 GHz, the Kamenetzky model consistently overestimates our data points. This gives that the Kamenetzky model predicts a steeper increase than we measure (Figure 2.6). While Kamenetzky's results came from the Z-Spec instrument at the Caltech Submillimeter Observatory (CSO), our DESHIMA 2.0 observations may have different beam characteristics.

Kamenetzky [15] explains that the continuum emission in NGC 1068 primarily comes from its SB ring. There are also contributions from the central disk and AGN jet ($\approx 10\%$). Importantly, the beam width of DESHIMA 2.0 changes significantly with frequency, narrowing as the frequency increases. Figure 3.7 indicates that the Full Width at Half Maximum (FWHM) of the DESHIMA 2.0 beam along its major axis decreases from about 27.02 arcseconds at 250 GHz to 23.49 arcseconds at 300 GHz, with the minor axis FWHM also narrowing from 25.89 arcseconds at 250 GHz to 22.65 arcseconds at 300 GHz. This change in beam size with frequency, especially at higher frequencies, affects how much of the extended SB ring emission we capture within our aperture. A narrower beam at higher frequencies would cover less of the continuum emission, which can clearly be seen in figure 3.6. However, for this all to be true the beam width of Z-spec on CSO should indeed be larger then that of DESHIMA 2.0 on ASTE. As can be seen in figure 3.8, the beam width of Z-spec is larger then that of DESHIMA 2.0 for the observation data [6], this validates our understanding of the differences between the observations. Therefore, the observed continuum will indeed be smaller compared to the model of Kamenetzky based on the observations of Z-spec on CSO.

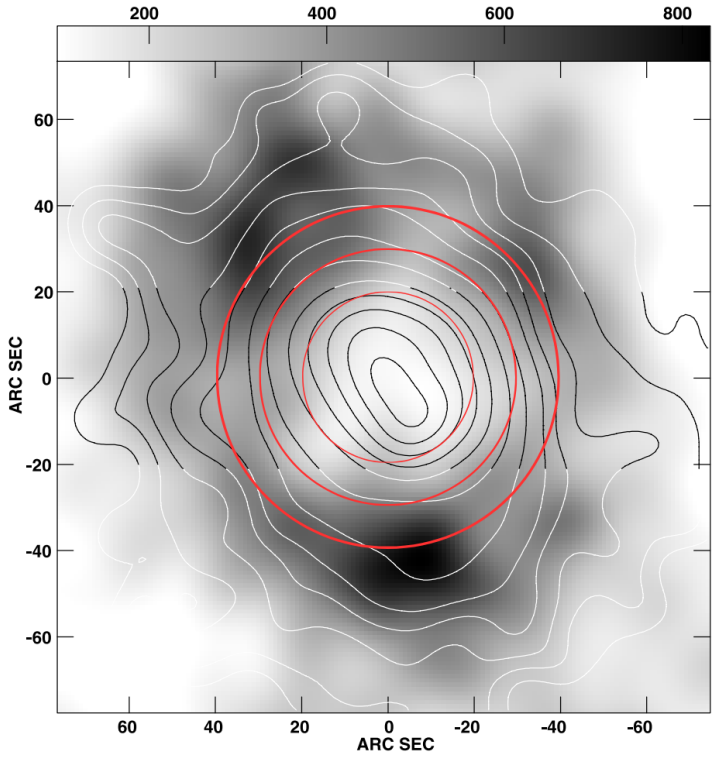

Figure 3.6: Continuum emission density of NGC 1068 [20]. The image displays velocity-integrated H I brightness in grayscale, with contours showing 850 μm (top) and 450 μm (bottom) continuum emission. Red labels indicate circles with diameters of 20, 30, and 40 arcseconds.

To reduce these beam-related effects and get the most reliable continuum parameters for our DESHIMA 2.0 data, we changed the MCMC fitting frequency range to 250 GHz to 280 GHz. We selected this range because it covers the main area emitting the continuum. This minimizes the effect of different beam coupling to the extended source and reduces the differences with earlier models at higher frequencies. This adjusted range helps us derive continuum parameters that better reflect the actual emission seen with DESHIMA 2.0.

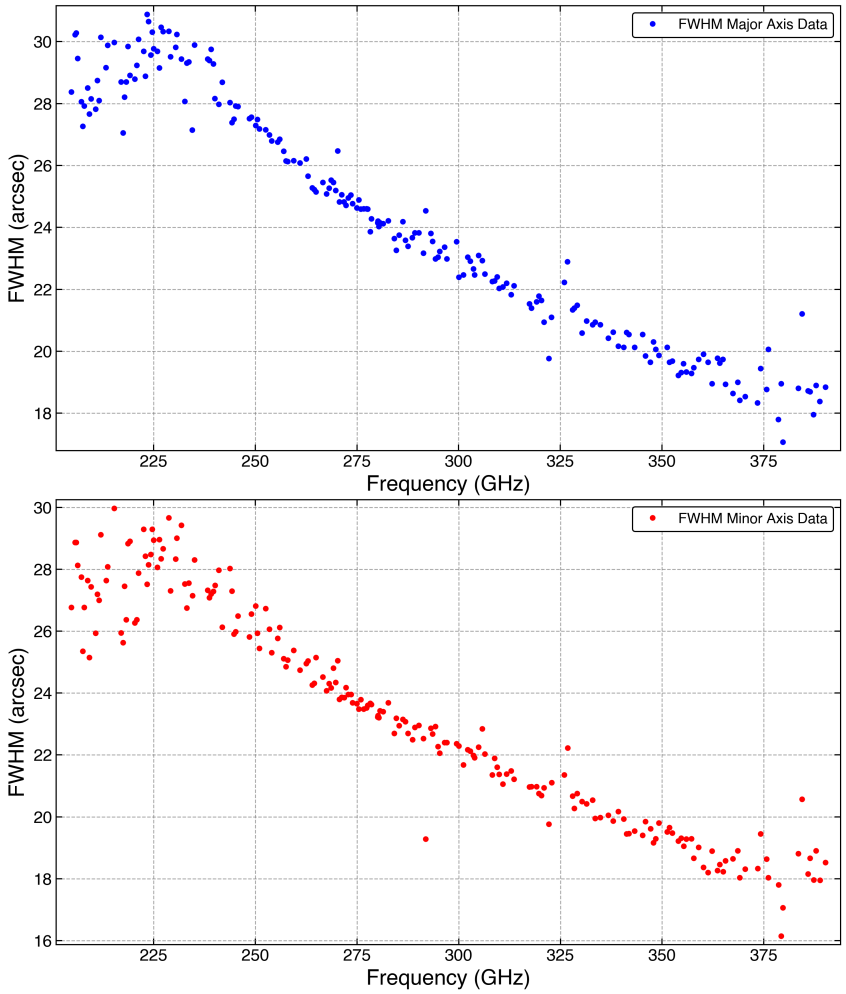

Figure 3.7: Plot 1 shows the beam width over the frequency range for the major axis, plot 2 shows the beam width over the frequency range for the minor axis. These beam widths are beam widths for DESHIMA 2.0 on ASTE [17]

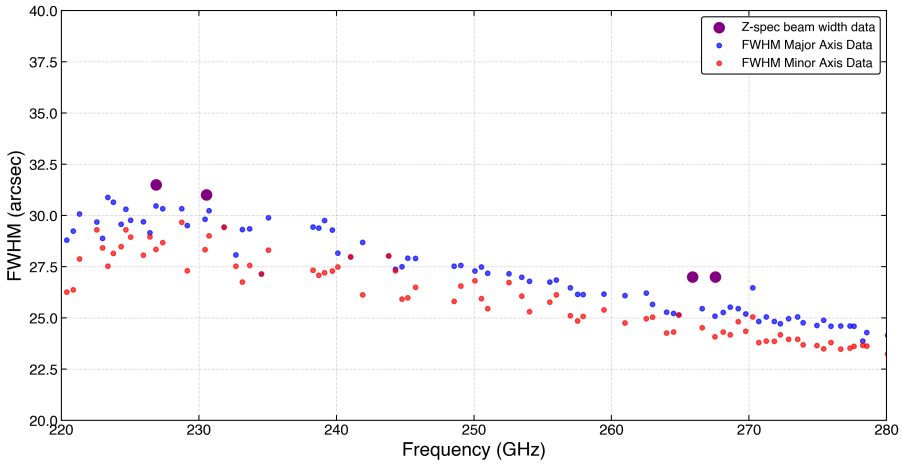

Figure 3.8: In this figure, the beam width of Z-spec attached to CSO [6] and of DESHIMA 2.0 on ASTE is plotted in arcseconds against the frequency in GHz. It can be seen that the beam width of Z-spec is larger at comparable frequencies.

3.2.5. Improved Continuum Fit: 250-280 GHz Range

With the refined frequency range of 250-280 GHz, the MCMC fitting procedure was re-executed. This section presents the results of this improved fit.

Chain convergence (250-280 GHz)
Similar to the first run, the MCMC chains for the 250-280 GHz range showed good convergence. All parameters used walkers initialized with the steps and burn-in period listed in table 2.2. As can be seen in the trace plot 3.9 the parameters converged well to an estimated continuum model parameter value. Figure 3.9 shows the trace plots, applying a burn-in of 2×10^4 steps. These plots display stable behaviour without significant trends. This confirms that the chains mixed well and accurately represent the posterior distribution for each parameter.

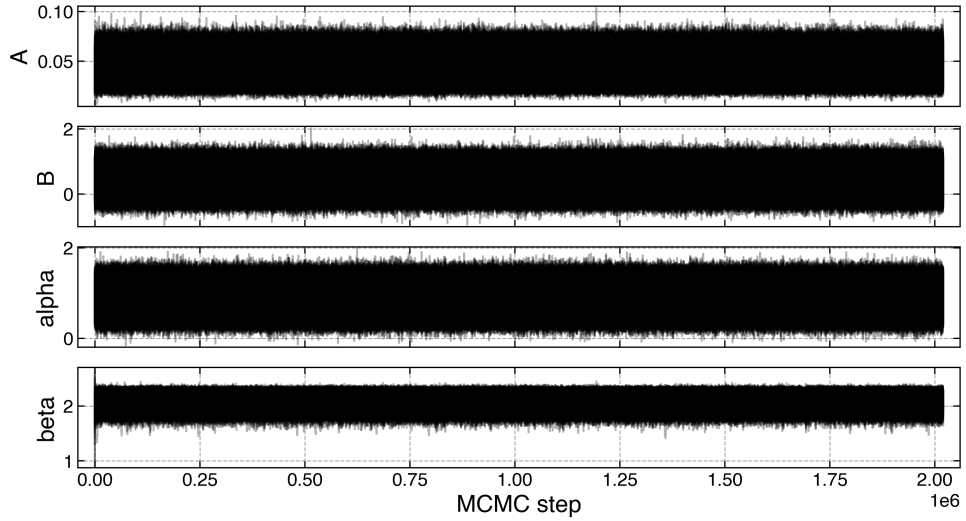

Figure 3.9: Trace plot showing how the MCMC sampler changes for the four free parameters of the continuum model (A, B, α, and β) over the 250-280 GHz range. After an initial burn-in phase, the chains mix well and show stability. This indicates that the sampler has converged to the posterior distribution.

Posterior distributions (250-280 GHz)
Table 3.2 presents the numerical results of the estimated parameters from the MCMC run in the refined frequency range.

Table 3.2: Posterior values for the MCMC run over the free continuum model parameters

Parameter	Mean (μ)	Std. Dev. (σ)
A	0.0441	± 0.0097
B	0.4392	± 0.258
α	0.9008	± 0.198
β	2.0941	± 0.091

The MCMC analysis for the 250-280 GHz range shows different levels of constraint across parameters. Parameter β has the highest precision at 4.3% relative uncertainty. It is followed by A and α, with 22% relative uncertainty. Parameter B shows the largest uncertainty at 59% relative uncertainty, indicating it is less well-constrained by the data.
Figure 3.10 shows the correlations between the free parameters. Most parameters show no correlation, which indicates strong parameter estimation. However, a positive correlation exists between A and β (approximately (Found value from the plot)). This correlation makes sense physically since (explain the physical relationship), suggesting these parameters may describe similar physical aspects.

Continuum model fit (250-280 GHz)
The continuum model from the MCMC run over the 250-280 GHz range is shown in figure 3.11.
The MCMC model, based on the Kamenetzky framework and derived from the obtained posterior values, resulted in an improvement for the reduced χ^2 value against the Kamenetzky values:

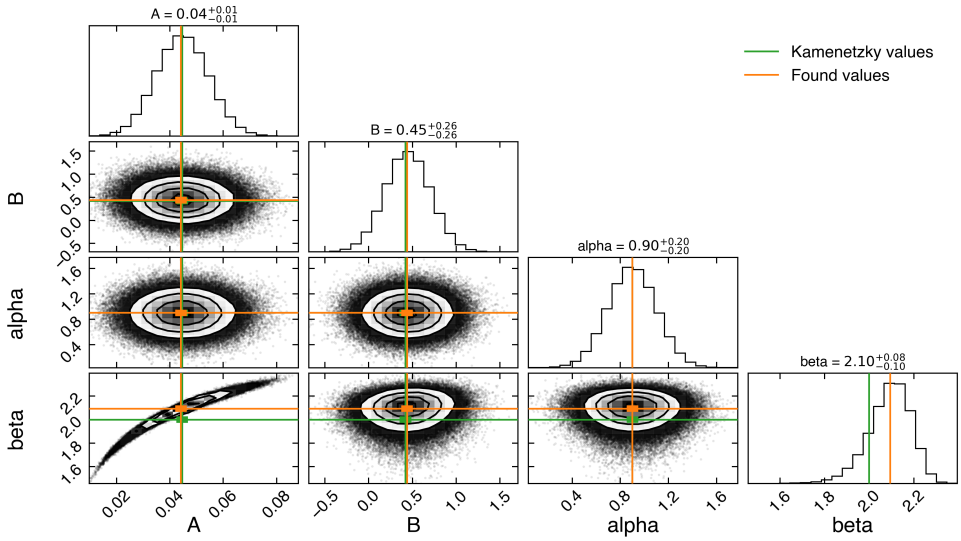

Figure 3.10: Marginalized posterior distributions for the continuum model parameters A, B, α, and β come from the MCMC sampling. The diagonal panels present the one-dimensional posteriors with the displayed median and 1σ uncertainties. The off-diagonal panels show the two-dimensional posterior distributions. The green lines indicate the prior (Kamenetzky) parameter values, while the orange lines represent the best-fit parameters from the MCMC run. The plot reveals possible correlations between parameters.

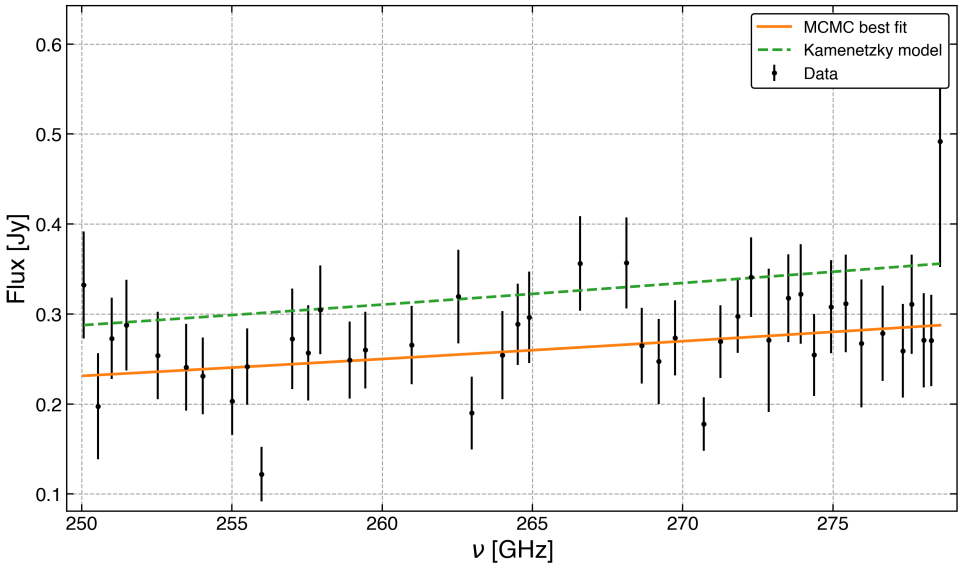

Figure 3.11: Observed flux data (black points with error bars) as a function of frequency (ν). The orange solid line represents the continuum model evaluated at the MCMC best-fit parameters. The dashed green line shows the model using the initial Kamenetzky (prior) parameter values.

- Reduced χ^2 for the MCMC best-fit model: 1.37
- Reduced χ^2 for the Kamenetzky values inserted into the model: 3.32

The MCMC model's reduced χ^2 value of 1.37 shows a good fit, indicating it captures the observed data well. In contrast, the Kamenetzky model's [15] reduced χ^2 of 3.32 suggests it underfits the data and does not account for the observed variability properly; however, it still gives a better approximation when compared to the initial frequency range continuum fit model.

The full continuum model using the posteriors found by the MCMC run can be seen in figure 3.12. As can be seen, the figure shows that for low frequencies (in the range between 250 - 300 GHz) the continuum model does describe the continuum obtained by the stacked spectrum of observation

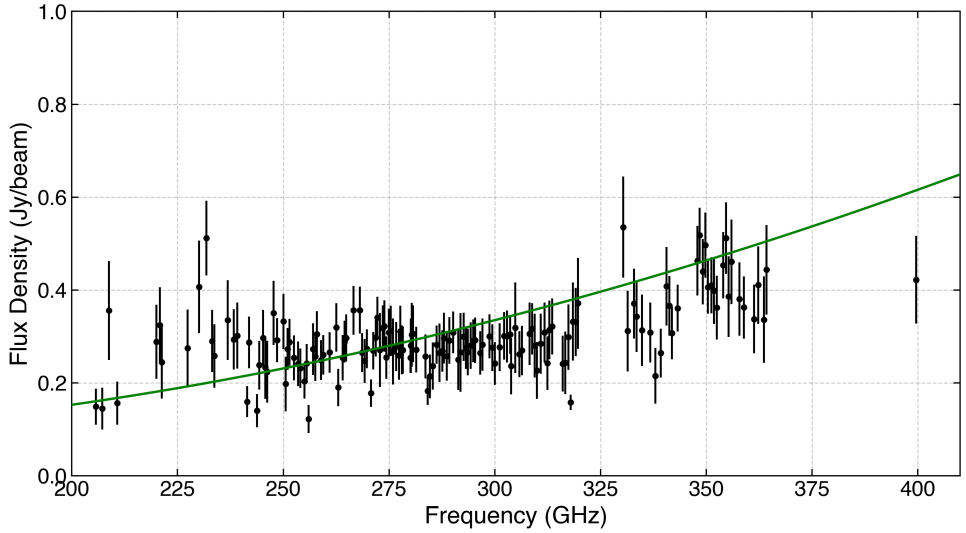

Figure 3.12: Observed flux density (black points with error bars) as a function of frequency the flux, the flux is limited for the points between 0 and 1 Jansky/beam. The solid green line shows the continuum model based on the best-fit parameters from the MCMC analysis, covering the entire frequency range. Note that the MCMC fit was done only on data between 250 and 280 GHz.

runs. However, with an increasing frequency the model gets more off to the continuum obtained by the observation runs.

3.2.6. Comparison to parameter values of Kamenetzky

This subsection provides a direct comparison of the continuum model parameters obtained from our MCMC analysis with the values reported by Kamenetzky [15], which also served as the basis for the prior distributions in our MCMC run.
Table 3.3 summarizes the mean and standard deviation for each parameter from both our MCMC results and the Kamenetzky model.

Table 3.3: Comparison of continuum model parameters from MCMC fit with Kamenetzky values.

Parameter	**Kamenetzky ($\mu \pm \sigma$)**	**MCMC ($\mu \pm \sigma$)**
A	0.0446 ± 0.0100	0.0441 ± 0.0097
B	0.4210 ± 0.2700	0.4392 ± 0.2580
α	0.9000 ± 0.2000	0.9008 ± 0.1980
β	2.0000 ± 0.5000	2.0941 ± 0.0910

Visually, the agreement between the MCMC derived model and the Kamenetzky model, along with their fit to the data, is shown in Figure 3.11. The MCMC best fit gives a good quantitative description of our data. This is clear from its reduced χ^2 value of 1.37, for the comparison to Kamenetzky's model we see an improvement in χ^2 to 3.32.

When we compare the individual parameter values in Table 3.3, our MCMC results closely match Kamenetzky's values within their respective uncertainties for parameters A, B, and α. The most significant difference occurs in the uncertainty for parameter β. Our MCMC analysis shows a much smaller standard deviation of ± 0.0910, while Kamenetzky's is ± 0.5.

3.2.7. Obtained spectra with continuum removed

Now that we have completed the characterization of the continuum and determined its model parameters using the MCMC method, the spectrum can be set up for the emission line analysis. From the stacked observation data (seen in figure 2.6) the continuum is subtracted from the stacked spectra. The resulting continuum-subtracted spectrum, which highlights the emission line features, is shown in figure 3.13.

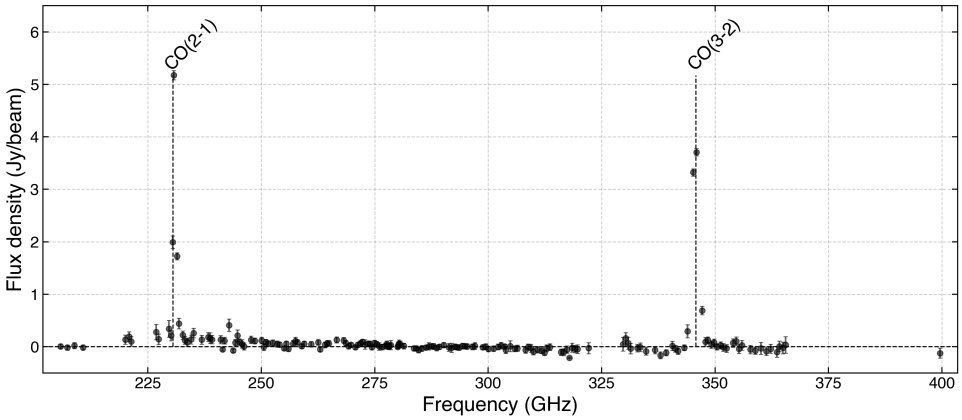

Figure 3.13: Continuum-subtracted stacked spectrum showing the emission line features. Black points represent observed flux density with error bars, with CO(2-1) and CO(3-2) lines visible at their expected frequencies.

3.3. Emission Line fitting Results

With the continuum characterised and removed from the stacked spectrum, as described in the last section and shown in Figure 3.13, the isolated emission line features can now be analysed. This section presents the results of the individual line fitting procedures described in the methodology. Derived properties of the observed molecular emission lines will be given, followed by direct comparison with values obtained from Z-spec observations by Qiu et al. [22].

As shown in Figure 3.13, the DESHIMA 2.0 data clearly show strong emission line features at the expected frequencies for the CO(2-1) and CO(3-2) molecular transitions. This visual evidence confirms that the dataset is appropriate for line fitting and further comparative analysis.

3.3.1. Voigt Profile Fitting

The Voigt profile fitting procedure was used on the emission lines seen in Figure 3.13. The visual results from the fitting process, explained in the methodology, are shown in Figure 3.14. The parameters from this fitting procedure are summarized in Table 3.4.

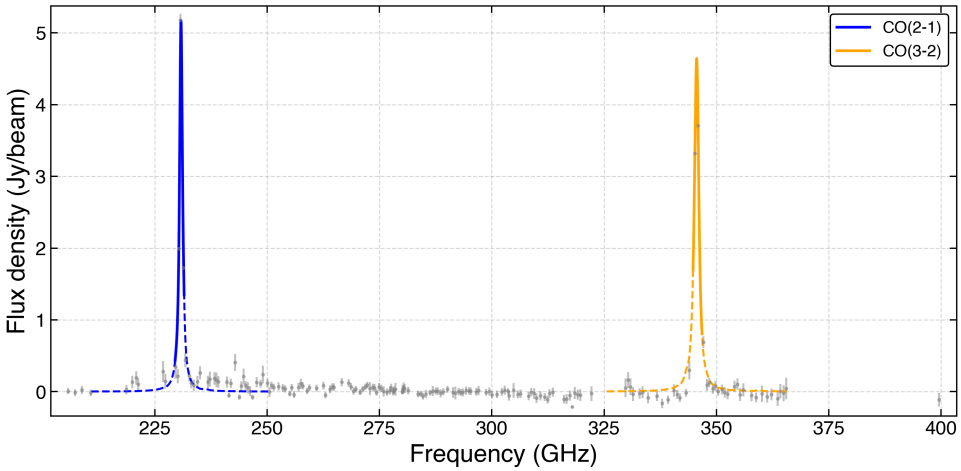

Figure 3.14: Voigt profile fits the observed molecular emission lines. The solid lines show the areas where the Voigt profile fitting took place. The dashed lines represent the extended Gaussian part of the fit used for flux integration. Grey dots represent the observed data points after subtracting the continuum.

As shown in Figure 3.14, the data points used for the line fitting procedure were intentionally limited to the area around the emission line features. This narrower fitting window was chosen to manage noise levels. The uncertainties of the obtained line parameters are notably large: the line width uncertainties

Table 3.4: Derived rotational transition emission line properties from Voigt profile fitting.

Transition	Frequency (GHz)	Flux (mK km/s)	Line width (km/s)	Main beam Temperature (mK)
CO(2-1)	230.8553 ± 0.0103	216976.0 ± 105327.0	305.80852 ± 148.3	170 ± 3.1
CO(3-2)	345.5763 ± 0.0101	185684.4 ± 38392.1	564.03887 ± 116.5	220 ± 1.9

are about 48% for CO(2-1) and 20.7% for CO(3-2), and the flux uncertainties are around 48% for CO(2-1) and 20.7% for CO(3-2).

3.3.2. Comparison to parameter values of Qiu

To evaluate the scientific capabilities of the single-pixel ISS DESHIMA 2.0, a direct comparison is made between the obtained values of the fitting procedure and Qiu [22]. This direct comparison is presented in Table 3.5.

Table 3.5: Comparison between the rotational transition emission line properties obtained by DESHIMA 2.0 with Voigt fitting and Qiu et a;. [22]. For the values of Qiu the weighted average was taken as stated in table 2.5.

Transition	Property	DESHIMA 2.0 (Voigt Fit)	Qiu et al. [22]	Ratio
CO(2-1)	Frequency (GHz)	230.8553 ± 0.0103	230.538	1.00
	Flux (mK km/s)	216976.0 ± 105327.0	203600 ± 20500	1.06
	Line width (km/s)	305.81 ± 148.3	116.5	2.63
	Main beam Temperature (mK)	170 ± 3.1	602.8	0.28
CO(3-2)	Frequency (GHz)	345.796	345.5763 ± 0.0101	1.00
	Flux (mK km/s)	185684.4 ± 38392.1	166000 ± 20000	1.12
	Line width (km/s)	564.04 ± 116.5	(-)	-
	Main beam Temperature (mK)	220 ± 1.9	630	0.35

The comparison in Table 3.5 presents the measured performance of DESHIMA 2.0 alongside established astronomical observations from Qiu et al. [22].

Frequency Accuracy For both CO(2-1) and CO(3-2) transitions, the central frequencies derived from DESHIMA 2.0 data are in good agreement with the reported values from Qiu et al. [22], with ratios of approximately 1.00.

Integrated Flux Consistency The integrated line fluxes for both CO(2-1) and CO(3-2) also show agreement with values from Qiu et al. [22], with ratios of approximately 1.07 and 1.12, respectively.

Line Profile Differences The main beam temperatures (T_{MB}) observed by DESHIMA 2.0 are consistently lower than those reported by Qiu et al. [22], with ratios of 0.28 for CO(2-1) and 0.35 for CO(3-2). The line width measured by DESHIMA 2.0 for CO(2-1) is notably broader, with a ratio of 2.63 compared to Qiu et al.'s weighted average. For CO(3-2), a direct comparison of line width was not possible as Qiu et al. did not report this value.

4

Discussion

This chapter interprets the results shown in Chapter 3. It provides context for the phenomena we observed and assesses the scientific capabilities of the DESHIMA 2.0 spectrometer. We will discuss how effective the data reduction process was. We will also look at the implications of the continuum fitting. Additionally, we will evaluate the emission line properties obtained from NGC 1068. We will pay special attention to the differences we noticed compared to existing literature. This discussion aims to combine the findings and their broader implications for future spectroscopic observations with DESHIMA 2.0.

4.1. Performance and validation of reduction process

In the reduction process, sigma clipping was applied, as well as a mask for the points with an SNR lower than 3. This resulted in a decrease in data points of 26% due to the sigma clipping, as well as 27%. However, this can be validated by the fact that these points were mainly deleted at atmospheric interference regions (200-205 GHz, around 325 Ghz and around 380 GHz), as can be seen in figure 3.1 and figure 3.2. However, as the filtering did manage to remove most outlier data, that would interfere with our results in a bad way. This still is a more agressive approach as 54% of the data points remain after filtering. This could lead to some valid data missing, which would have created more reliable estimated parameters regarding the line fitting, for example. However, the estimation of the free continuum model parameters was done over a larger array of data. Therefore, that effect was minimized.

4.2. Interpretation and Validation of continuum measurements

This section will give insights into the meaning of the continuum fitting results and their implications for DESHIMA 2.0's measurement abilities.

4.2.1. MCMC Fit Robustness and Parameter Constraints

The values from our MCMC continuum fitting in the range of 250-280 GHz are similar to those reported by Kamenetzky, showing a good match with existing literature. However, the uncertainties in B and alpha are 58% and 22% respectively. This suggests a high sensitivity due to the characteristics of the data. The uncertainty might be related to the variability of the data points themselves or the fact that the reduction process eliminated too many points. Unlike Kamenetzky's findings regarding the relationship between B and β, which were found to be degenerate, we discovered a different relationship: B and β were not degenerate.

In addition to the constraints on individual parameters, the corner plot analysis, found in Figures 3.10 and 3.10, shows a positive correlation between parameters A and β. This relationship can be understood by looking at the functional form of our continuum model, which describes the flux density as:

$$F_\nu \propto A\Omega T \nu_0^{-\beta} \nu^{B+\beta} \tag{4.1}$$

In this model, A is the amplitude scaling factor for the flux density, setting the baseline of the continuum. At the same time, β explains how dust emissivity changes with frequency, defining the spectral slope.

The observed positive correlation between A and β indicates a form of degeneracy within the model: an increase in overall continuum brightness (A) can be offset by a corresponding increase in the spectral slope (β) to maintain a good fit to the observed data. This means that both parameters work together to shape the intensity and spectral characteristics of the continuum emission across the observed band.

4.2.2. The Role of Beam Characteristics in Continuum Modelling

As explained in section 3.2.4, we adjusted the frequency fitting region to 250-280 GHz. Ideally, the same method would have been applied to data from DESHIMA 2.0 on ASTE as Kamenetzky used for Z-spec on CSO. We suspect that a more accurate and better description of the continuum for DESHIMA 2.0 data could be achieved if the continuum was fitted over a longer frequency range, for example, 200-400 GHz, with a reduction of high noise data. However, this was not the goal for the continuum fitting in this thesis. Therefore, for the purpose of comparison, a comparison between the free continuum model parameters from the 250-280 GHz range provides a more accurate description that overlaps with Kamenetzky's values. We can elaborate on this because the reduced χ^2 value decreased from the earlier 4.54 for the 250-300 GHz range to 3.32 for the 250-280 GHz range.

4.3. Interpretation of emission line fitting

This section will interpret the results for the emission line fitting, focussing on DESHIMA's ability to accurately describe line emissions.

4.3.1. Voigt Profile Fit Quality and Impact of Data Limitations

Visually, the line fitting has a good fit quality, as shown in figure 3.14. While the visual results demonstrate reasonable fits to the emission line features, the analysis obtained high uncertainties in the values for the line width and, therefore, the integrated flux density too (Table 3.4). These uncertainties primarily arise because of the limit on using data points around the centre frequency (as seen in figure 3.14). This narrow fitting was chosen to mitigate high noise level features in the so-called 'wings' surrounding the emission line. Therefore, a broader fitting range would have increased the noise and, thereby, the uncertainties of the obtained parameters. For example, we see that for the CO(2-1) emission line in the wings of the Voigt profile, there is more noise in the data points than in the range between 250-310 GHz range. When this noise can be limited or extracted, the uncertainties in the obtained parameters will likely be smaller. However, as a result, the uncertainties of the obtained line parameters are quite significant. These relatively large uncertainties directly reflect the SNR limitations of the current dataset. While a fit was achieved, the overall quality for constraining individual line shape parameters (like precise linewidths and peak temperatures) is limited by these noise characteristics as shown in table 3.4, indicating a need for improved data quality in future observations to enhance precision.

A further complication adds to the uncertainty, specifically for the CO(2-1) line. The DESHIMA instrument was initially designed for a frequency range of 220-440 GHz but that was later changed to 200-400 GHz. This change, however, created a problem in the 200-240 GHz range. In this range the filter banks measure a frequency and its second harmonic. This means that for any frequency in this range, the instrument measures a mix of the power of this frequency and its second harmonic. This effect raises the antenna temperature, leading to higher uncertainty in the measured flux. Since the CO(2-1) line is at 230.538 GHz, it falls within this problematic range, which explains the larger uncertainties seen for this specific emission line.

4.3.2. Interpreting Line profile discrepancies

While the integrated line fluxes from the data of DESHIMA 2.0 on ASTE showed good agreement with those reported by Qiu et al. [22], the obtained differences in peak main beam temperature and the line widths ask for further discussion. These differences in values can primarily be explained by two factors: instrumental beam characteristics and line fitting methodologies.

Instrumental beam characteristics Firstly, different instrumental beam widths significantly affect our measurements. DESHIMA 2.0 observed CO(2-1) and CO(3-2) with beam widths of about 27.5 and 20 arcseconds, respectively. In contrast, Papadopoulos et al. [20] used narrower beams of 21 and 14 arcseconds for the same transitions. A larger beam covers a larger area for an extended source like

NGC 1068, whose CO emission is concentrated in the centre 1.4. This leads to ”beam dilution,” causing a lower observed main beam temperature (T_{mb}) for DESHIMA 2.0 because it averages bright emission with fainter regions.

Similarly, the larger beam captures a broader range of velocities from the galaxy's complex internal motions (e.g., rotation). This integration causes the observed line profile to broaden, an effect known as ”beam smearing” [10]. While beam smearing likely contributes to the increased line width, a ratio of 2.63 for CO(2-1) compared to Qiu et al. [22] would be too high. This difference also reveals the impact of different line fitting methods and possible uncertainties. A more reliable comparison could be made when the circumstances are alike, and the approaches are consistent with each other.

Different line fitting methods Secondly, a crucial factor in the differences in the derived emission line properties comes from the different methods used. Our analysis used a single-component Voigt profile to fit the observed emission lines. In contrast, Qiu et al. [22] used a more complicated three-component Gaussian fit to model the CO(2-1) line. They specifically considered the complex kinematics of NGC 1068.

When a single Voigt profile is applied to a spectrum that is made up of multiple distinct kinematic components, like those in NGC 1068, the fitting process tries to include all these components within one broad profile. This leads to a significantly wider derived line width. Additionally, for a given integrated line flux, which we found to be mostly consistent between the studies, a broader line profile results in a lower peak main beam temperature (T_{mb}) to maintain the total area under the line. Thus, this method difference explains the wider line widths and lower main beam temperatures seen in our DESHIMA 2.0 data compared to Qiu et al.'s multi-component analysis.

Conclusion on best comparison metric Given the complexities that arise from differing instrumental beam characteristics and line fitting methods, it becomes clear that the integrated flux density is the most reliable parameter for direct comparison between observations of DESHIMA 2.0 on ASTE and existing literature, like that of Qiu et al. [22]. This parameter is the least sensitive to the model use and specific observation parameters.

5

Conclusion

This study asessed the scientific capabilities of DESHIMA 2.0 that made observation runs when attached to ASTE by comparing to literature. The observations made by DESHIMA 2.0 on ASTE are in line with literature. The results however, also highlight areas that will need further refinement.

The data reduction, despite the aggressive approach, did successfully prepare the spectrum for further analyses.

In the 250-280 GHz range, DESHIMA 2.0's estimated free continuum model parameters (A, B, β, α) aligned well with Kamenetzky (2011) [15] and established literature, also obtaining an A-β correlation. However, across the wider 250-300 GHz frequency range, the derived parameters showed less consistency with Kamenetzky's findings, a difference that variations in beam width explained.

The spectrometer accurately measured the central frequencies of the CO(2-1) and CO(3-2) emission lines. It provided integrated line fluxes close to the literature observed line fluxes [22]. Establishing this as the most reliable metric for direct comparison. However, there were discrepancies in the main beam temperatures and the line width in the literature. However, these discrepancies could be explained by combining beam dilution/smearing effects and differing line fitting methods.

The study provided a clearer understanding of the capabilities of DESHIMA 2.0, showing consistency with literature in certain areas. DESHIMA 2.0 did establish the ability to derive the continuum by showing a good agreement with the existing studies [15]. The study also demonstrated the capacity of the single pixel ISS to reliably measure integrated line fluxes by showing consistency with the reported values by existing studies [22]. The detailed analysis of the line profile discrepancies provides insights for future spectroscopic data observed by DESHIMA 2.0. Overall, the findings contribute to a better understanding of DESHIMA 2.0

This study points out the limitations of the current dataset and observational method. First, the reduction of data, which removed 46% of data points, increased uncertainties in the derived parameters, particularly in line fitting. Second, using a single Voigt profile for line fitting, rather than the multi-component approaches used in other studies, made it hard to directly compare line shape properties such as peak temperatures and line widths beyond the total integrated flux. Third, while the continuum model was validated against the literature in the 250-280 GHz range, a full characterization of the continuum across the entire observed bandwidth (200-400 GHz) was not performed in this study. This limits the derivation of the full continuum of DESHIMA 2.0. The choice of NGC 1068, while it provided a valuable test case, introduced challenges for direct comparison with its spatially varying properties for both the emission lines and the continuum emission.

5.1. Recommondations and Future Prospects

To improve the verification of the scientific capabilities of DESHIMA 2.0, several recommendations can be made for future work. First, future observations could aim for longer integration times for an

improvement of SNR and reduce uncertainties in line parameters. Also, alternative or adaptive filtering techniques could be explored to minimize the loss of valid data points while still removing noise from the already observed data. Also, a more advanced modelling technique that accounts for the telescope's beam and source morphology can be used when analyzing extended sources.

Further investigation in different well studied galaxies can also lead to a better understanding of DESHIMA 2.0's capabilities. By observing astronomical sources with different properties, like different dust content and different bright emission line features, and comparing them with existing well-studied data, we can verify the instrument's scientific capabilities in different settings. This will also showcase how beam characteristics and fitting methods change measurements for different astronomical sources.

Acknowledgements

First of all, I would like to express my gratitude to the entire Experimental Astronomy group for helping me feel part of a research team. Attending the bi-weekly meetings with the DESHIMA team provided me insights into the operations of an experimental research group. Especially, I want to thank Akira, whose guidance and introduction to the team made me feel that my contributions were valued. Whenever I encountered difficulties, for example with the line-fitting procedure, the DESHIMA team assisted me toward the solutions.

I also want to thank Arend, the weekly meetings (sometimes on the very warm friday afternoons) gave me insights to how the DESHIMA instruments works and explained how the physics and processing behind observing the universe works. While I was already interested in the working of the universe and how we as humans are exploring it step by step, this made me even more excited!

Additionally, I would like to thank Arend for providing data and models, improving my ability to evaluate the observed spectra. While implementing certain aspects of the code was sometimes challenging, his help made the process considerably more doable.

Thank you all for making this project an unforgettable and impactful experience. I have learned a lot along the way.

Bibliography

[1] A Amvrosiadis et al. “The kinematics of massive high-redshift dusty star-forming galaxies”. In: *Monthly Notices of the Royal Astronomical Society* 536.4 (Dec. 2024), pp. 3757–3783. ISSN: 1365-2966. DOI: 10.1093/mnras/stae2760. URL: http://dx.doi.org/10.1093/mnras/stae2760.

[2] Armando Azua-Bustos, Catalina Urrejola, and Rafael Vicuña. “Life at the dry edge: Microorganisms of the Atacama Desert”. In: *FEBS Letters* 586.18 (July 2012), pp. 2939–2945. ISSN: 1873-3468. DOI: 10.1016/j.febslet.2012.07.025. URL: http://dx.doi.org/10.1016/j.febslet.2012.07.025.

[3] A Blain. “Submillimeter galaxies”. In: *Physics Reports* 369.2 (Oct. 2002), pp. 111–176. ISSN: 0370-1573. DOI: 10.1016/s0370-1573(02)00134-5. URL: http://dx.doi.org/10.1016/S0370-1573(02)00134-5.

[4] James J. Condon and Scott M. Ransom. “Chapter 7: Spectral Lines”. In: *Essential Radio Astronomy*. National Radio Astronomy Observatory, 2018. URL: https://www.cv.nrao.edu/~sransom/web/Ch7.html.

[5] E. da Cunha et al. “AN ALMA SURVEY OF SUB-MILLIMETER GALAXIES IN THE EXTENDED-CHANDRADEEP FIELD SOUTH: PHYSICAL PROPERTIES DERIVED FROM ULTRAVIOLET-TO-RADIO MODELING”. In: *The Astrophysical Journal* 806.1 (June 2015), p. 110. ISSN: 1538-4357. DOI: 10.1088/0004-637x/806/1/110. URL: http://dx.doi.org/10.1088/0004-637X/806/1/110.

[6] L. Earle et al. “Z-Spec: a broadband direct-detection millimeter-wave spectrometer – instrument status and first results”. In: ed. by Jonas Zmuidzinas et al. Orlando, Florida , USA, June 2006, p. 627510. DOI: 10.1117/12.672309. URL: http://proceedings.spiedigitallibrary.org/proceeding.aspx?doi=10.1117/12.672309 (visited on 06/25/2025).

[7] Akira Endo et al. “First light demonstration of the integrated superconducting spectrometer”. en. In: *Nature Astronomy* 3.11 (Aug. 2019), pp. 989–996. ISSN: 2397-3366. DOI: 10.1038/s41550-019-0850-8. URL: https://www.nature.com/articles/s41550-019-0850-8 (visited on 05/27/2025).

[8] Akira Endo et al. “Wideband on-chip terahertz spectrometer based on a superconducting filterbank”. In: *Journal of Astronomical Telescopes, Instruments, and Systems* 5.03 (June 2019), p. 1. ISSN: 2329-4124. DOI: 10.1117/1.jatis.5.3.035004. URL: http://dx.doi.org/10.1117/1.JATIS.5.3.035004.

[9] Daniel Foreman-Mackey et al. “<tt>emcee</tt>: The MCMC Hammer”. In: *Publications of the Astronomical Society of the Pacific* 125.925 (Mar. 2013), pp. 306–312. ISSN: 1538-3873. DOI: 10.1086/670067. URL: http://dx.doi.org/10.1086/670067.

[10] Karl Glazebrook. “The Dawes Review 1: Kinematic Studies of Star-Forming Galaxies Across Cosmic Time”. In: *Publications of the Astronomical Society of Australia* 30 (2013). ISSN: 1448-6083. DOI: 10.1017/pasa.2013.34. URL: http://dx.doi.org/10.1017/pasa.2013.34.

[11] Jonathan Goodman and Jonathan Weare. “Ensemble samplers with affine invariance”. In: *Communications in Applied Mathematics and Computational Science* 5.1 (Jan. 2010), pp. 65–80. ISSN: 1559-3940. DOI: 10.2140/camcos.2010.5.65. URL: http://dx.doi.org/10.2140/camcos.2010.5.65.

[12] C. Gruppioni. “The Herschel□ PEP/HerMES luminosity function – I. Probing the evolution of PACS selected Galaxies to z □ 4”. In: *Monthly Notices of the Royal Astronomical Society* 432.1 (Apr. 2013), pp. 23–52. ISSN: 0035-8711. DOI: 10.1093/mnras/stt308. URL: http://dx.doi.org/10.1093/mnras/stt308.

[13] W. K. Hastings. “Monte Carlo sampling methods using Markov chains and their applications”. In: *Biometrika* 57.1 (Apr. 1970), pp. 97–109. ISSN: 0006-3444. DOI: 10.1093/biomet/57.1.97. URL: http://dx.doi.org/10.1093/biomet/57.1.97.

[14] John P. Huchra, Michael S. Vogeley, and Margaret J. Geller. “The CfA Redshift Survey: Data for the South Galactic Cap”. In: *The Astrophysical Journal Supplement Series* 121.2 (Apr. 1999), pp. 287–368. ISSN: 1538-4365. DOI: 10.1086/313194. URL: http://dx.doi.org/10.1086/313194.

[15] J. Kamenetzky et al. “The Dense Molecular Gas in the Circumnuclear Disk of NGC 1068”. In: *The Astrophysical Journal* 731 (2011). DOI: 10.1088/0004-637X/731/2/83.

[16] M. Krips et al. “A Multi□Transition HCN and HCO+Study of 12 Nearby Active Galaxies: Active Galactic Nucleus versus Starburst Environments”. In: *The Astrophysical Journal* 677.1 (Apr. 2008), pp. 262–275. ISSN: 1538-4357. DOI: 10.1086/527367. URL: http://dx.doi.org/10.1086/527367.

[17] A. Moerman et al. “Optimisation-based alignment of wide-band integrated superconducting spectrometers for submillimeter astronomy”. en. In: *Astronomy & Astrophysics* 684 (Apr. 2024). Publisher: EDP Sciences, A161. ISSN: 0004-6361, 1432-0746. DOI: 10.1051/0004-6361/202348525. URL: https://www.aanda.org/articles/aa/abs/2024/04/aa48525-23/aa48525-23.html (visited on 06/02/2025).

[18] National Aeronautics and Space Administration. *Active Galaxy NGC 1068*. https://science.nasa.gov/image-detail/ngc-1068/. Image Credit: NASA, ESA, Alex Filippenko (UC Berkeley), William Sparks (STScI), Luis C. Ho (KIAA-PKU), Matthew A. Malkan (UCLA), Alessandro Capetti (STScI); Image Processing: Alyssa Pagan (STScI). Sept. 2024.

[19] H. Nguyen et al. “Z-Spec’s first light at the Caltech Submillimeter Observatory”. In: *Nuclear Instruments and Methods in Physics Research Section A: Accelerators, Spectrometers, Detectors and Associated Equipment* 559.2 (Apr. 2006), pp. 626–628. ISSN: 0168-9002. DOI: 10.1016/j.nima.2005.12.123. URL: http://dx.doi.org/10.1016/j.nima.2005.12.123.

[20] Padeli P. Papadopoulos and E. R. Seaquist. “The State of the Molecular Gas in a Luminous Starburst/Seyfert 2 Galaxy: NGC 1068 Revisited”. In: *The Astrophysical Journal* 516.1 (May 1999), pp. 114–126. ISSN: 1538-4357. DOI: 10.1086/307090. URL: http://dx.doi.org/10.1086/307090.

[21] Madelief Peters. *Evaluating the On-Sky Sensitivity of DESHIMA 2.0: Chasing the Photon-Noise Limit in Submillimetre Astronomy*. Bachelor of Science in Applied Physics. 2024.

[22] Jianjie Qiu et al. “λ= 2 mm spectroscopy observations toward the circumnuclear disk of NGC 1068”. In: *Astronomy and Astrophysics* 634 (Feb. 2020), A125. ISSN: 1432-0746. DOI: 10.1051/0004-6361/201935800. URL: http://dx.doi.org/10.1051/0004-6361/201935800.

[23] Joris van Rantwijk et al. “Multiplexed Readout for 1000-Pixel Arrays of Microwave Kinetic Inductance Detectors”. In: *IEEE Transactions on Microwave Theory and Techniques* 64.6 (June 2016), pp. 1876–1883. ISSN: 1557-9670. DOI: 10.1109/tmtt.2016.2544303. URL: http://dx.doi.org/10.1109/TMTT.2016.2544303.

[24] D. B. Sanders et al. “TheIRASRevised Bright Galaxy Sample”. In: *The Astronomical Journal* 126.4 (Oct. 2003), pp. 1607–1664. ISSN: 1538-3881. DOI: 10.1086/376841. URL: http://dx.doi.org/10.1086/376841.

[25] E. Schinnerer et al. “Bars and Warps Traced by the Molecular Gas in the Seyfert 2 Galaxy NGC 1068”. In: *The Astrophysical Journal* 533.2 (Apr. 2000), pp. 850–868. ISSN: 1538-4357. DOI: 10.1086/308702. URL: http://dx.doi.org/10.1086/308702.

[26] Ian Smail, R. J. Ivison, and A. W. Blain. “A Deep Submillimeter Survey of Lensing Clusters: A New Window on Galaxy Formation and Evolution”. In: *The Astrophysical Journal* 490.1 (Nov. 1997), pp. L5–L8. ISSN: 0004-637X. DOI: 10.1086/311017. URL: http://dx.doi.org/10.1086/311017.

[27] Luigi Spinoglio et al. “The Far□Infrared Emission Line and Continuum Spectrum of the Seyfert Galaxy NGC 1068”. In: *The Astrophysical Journal* 623.1 (Apr. 2005), pp. 123–136. ISSN: 1538-4357. DOI: 10.1086/428495. URL: http://dx.doi.org/10.1086/428495.

[28] Tatsuya Takekoshi et al. “DESHIMA on ASTE: On-Sky Responsivity Calibration of the Integrated Superconducting Spectrometer”. en. In: *Journal of Low Temperature Physics* 199.1-2 (Apr. 2020), pp. 231–239. ISSN: 0022-2291, 1573-7357. DOI: 10.1007/s10909-020-02338-0. URL: http://link.springer.com/10.1007/s10909-020-02338-0 (visited on 06/24/2025).

[29] Akio Taniguchi et al. “DESHIMA 2.0: Development of an Integrated Superconducting Spectrometer for Science-Grade Astronomical Observations”. In: *Journal of Low Temperature Physics* 209.3–4 (Nov. 2022), pp. 278–286. ISSN: 1573-7357. DOI: 10.1007/s10909-022-02888-5. URL: http://dx.doi.org/10.1007/s10909-022-02888-5.

[30] GNU Astronomy Utilities. *Sigma-clipping*. GNU Project. 2024. URL: https://www.gnu.org/software/gnuastro/manual/html_node/Sigma-clipping.html.

Appendices

A

Continuum fitting code

```python
import os
import sys
import numpy as np
import matplotlib.pyplot as plt
import corner
from astropy import constants as const
import emcee
from matplotlib.lines import Line2D
from matplotlib.patches import Rectangle

# Apply project styling (which may enable a grid by default)
sys.path.append(os.path.dirname(os.path.dirname(os.path.abspath(__file__))))
from Plotting import plot_settings

# Settings for MCMC fit
ROOT = "Data/npys"
MASK_MIN, MASK_MAX = 250, 300
PRIOR = {
    'A': (4.46e-2, 0.001 * 10),
    'B': (0.421, 0.027 * 10),
    'alpha': (0.9, 0.2),
    'beta': (2.0, 0.5),
}
N_WALK, N_BURN, N_RUN = 32, 20000, 2000000

# Telescope constants
D = 10.0
etaA = 0.45
kB = const.k_B.value
Ae = etaA * np.pi * (D / 2) ** 2
conv = 2 * kB / Ae / 1e-26

# Model constants
T, NU0, OMEGA, F0 = 34.0, 3000.0, 1.66e-8, 0.028

# Planck function to compute blackbody radiation at given frequency
def planck(nu):
    nu_hz = nu * 1e9  # Convert GHz to Hz
    x = const.h.value * nu_hz / (const.k_B.value * T)
```

```
    B_si = 2.0 * const.h.value * nu_hz ** 3 / const.c.value ** 2 / np.expm1(x)
    return B_si * 1e26  # Return in Jy per beam

# Kamenetzky model for the continuum
def model(nu, A, B, alpha, beta):
    gb = A * (nu / 240) ** (B - 2) * OMEGA * planck(nu) * (1 - np.exp(-(nu / NU0)
        ** beta))
    cj = F0 * (nu / 230) ** (-alpha)
    return gb + cj

# This function computes the log prior of the model parameters
def ln_prior(p):
    A, B, alpha, beta = p
    if A < 0 or beta < 0:
        return -np.inf  # If any parameter is out of bounds, return -infinity
    lp = 0.0
    for v, (c, q) in zip(p, PRIOR.values()):
        lp += -0.5 * ((v - c) / q) ** 2 - np.log(np.sqrt(2 * np.pi) * q)  #
            Gaussian prior
    return lp

# This function computes the log likelihood of the model given the data
def ln_like(p, nu, f, var):
    m = model(nu, *p)  # Get the model values for the parameters
    return -0.5 * np.sum((f - m) ** 2 / var + np.log(2 * np.pi * var))  #
        Likelihood function

# This function combines the prior and likelihood to compute the log posterior
def ln_post(p, nu, f, var):
    lp = ln_prior(p)  # Log prior
    if not np.isfinite(lp):
        return -np.inf  # If prior is invalid, return -infinity
    return lp + ln_like(p, nu, f, var)  # Log posterior

# Load the data from the folder
def load(folder):
    nu = np.load(os.path.join(folder, 'freq.npy'))
    Tb = np.load(os.path.join(folder, 'avg.npy'))
    varT = np.load(os.path.join(folder, 'var.npy'))
    mask = (nu >= MASK_MIN) & (nu <= MASK_MAX)
    good = mask & np.isfinite(Tb) & np.isfinite(varT) & (varT > 0)
    if not np.any(good):
        raise RuntimeError("No continuum points after masking")
    nu, Tb, varT = nu[good], Tb[good], varT[good]
    S = conv * Tb  # Convert temperature to flux density
    varS = (conv ** 2) * varT  # Variance of the flux density
    return nu, S, varS

# Main function to run the MCMC fitting
def run(folder):
    nu, flx, var = load(folder)

    # Initialize walkers
    p0 = [[np.random.normal(c, q) for c, q in PRIOR.values()] for _ in range(
        N_WALK)]
    sampler = emcee.EnsembleSampler(N_WALK, len(PRIOR), ln_post, args=(nu, flx,
        var))
    sampler.run_mcmc(p0, N_BURN + N_RUN, progress=True)

    # Compute autocorrelation times (if possible)
    try:
```

```
        tau = sampler.get_autocorr_time(discard=N_BURN)
        print("Autocorrelation times per parameter:")
        for name, t in zip(PRIOR.keys(), tau):
            print(f"  {name}: {t:.1f} steps")
    except Exception as e:
        print("Warning: could not compute autocorr_time:", e)

    # Thinning and flattening the chain for best fit
    flat_chain = sampler.get_chain(discard=N_BURN, thin=100, flat=True)
    flat_lp = sampler.get_log_prob(discard=N_BURN, thin=100, flat=True)
    best_idx = np.argmax(flat_lp)
    best = flat_chain[best_idx]
    params = dict(zip(PRIOR.keys(), best))

    # Compute interval uncertainties
    p16, p50, p84 = np.percentile(flat_chain, [16, 50, 84], axis=0)
    perr_minus = p50 - p16
    perr_plus = p84 - p50

    print("Parameter estimates (median σ+1 / σ-1):")
    for i, name in enumerate(PRIOR.keys()):
        print(f"  {name} = {p50[i]:.4f} (+{perr_plus[i]:.4f}/-{perr_minus[i]:.4f})
            ")

    prior_truths = np.array([c for (c, q) in PRIOR.values()])
    found_truths = np.array(best)

    # Corner plot with prior and found values
    ndim = len(PRIOR)
    fig = corner.corner(
        flat_chain,
        labels=list(PRIOR.keys()),
        show_titles=True,
        title_kwargs={"fontsize": 12},
        show_grid=False  # cornerinternal grid off
    )
    axes = np.array(fig.axes).reshape((ndim, ndim))

    for i in range(ndim):
        for j in range(ndim):
            axes[i, j].grid(False)

    # Overplot kamenetzky (prior) and found values
    for i in range(ndim):
        ax_diag = axes[i, i]
        ax_diag.axvline(prior_truths[i], color='#2ca02c', ls='-', zorder=10)
        ax_diag.axvline(found_truths[i], color='C1', ls='-', zorder=11)

        for j in range(i):
            ax = axes[i, j]
            ax.axvline(prior_truths[j], color='#2ca02c', ls='-', zorder=10)
            ax.axhline(prior_truths[i], color='#2ca02c', ls='-', zorder=10)
            ax.axvline(found_truths[j], color='C1', ls='-', zorder=11)
            ax.axhline(found_truths[i], color='C1', ls='-', zorder=11)

            # Create rectangles around the prior and found values for style
            xlim = ax.get_xlim()
            ylim = ax.get_ylim()
            dx = 0.05 * (xlim[1] - xlim[0])
            dy = 0.05 * (ylim[1] - ylim[0])
```

```
            rect_p2 = Rectangle(
                (prior_truths[j] - dx / 2, prior_truths[i] - dy / 2),
                dx, dy,
                facecolor='#2ca02c', alpha=1,
                edgecolor='#2ca02c', lw=1,
                zorder=10
            )
            rect_f2 = Rectangle(
                (found_truths[j] - dx / 2, found_truths[i] - dy / 2),
                dx, dy,
                facecolor='C1', alpha=1,
                edgecolor='C1', lw=1,
                zorder=11
            )
            ax.add_patch(rect_p2)
            ax.add_patch(rect_f2)

    # Legend for prior and found values
    prior_handle = Line2D([], [], color='#2ca02c', ls='-', label='Kamenetzky
        values')
    found_handle = Line2D([], [], color='C1', ls='-', label='Found values')
    fig.legend(
        handles=[prior_handle, found_handle],
        loc='upper right',
        fontsize=14,
        frameon=False,
        bbox_to_anchor=(0.95, 0.95),
        bbox_transform=fig.transFigure
    )

    plt.show()
    plt.close(fig)

    # Create a plot of the best fit model and data
    plt.figure(figsize=(10, 6))
    plt.errorbar(nu, flx, yerr=np.sqrt(var), fmt='.k', label='Data')

    nu_s = np.linspace(nu.min(), nu.max(), 200)
    # MCMC best fit
    plt.plot(nu_s, model(nu_s, *best), 'C1-', lw=2, label='MCMC best fit')
    # Kamenetzky (prior) fit
    plt.plot(nu_s, model(nu_s, *prior_truths), '--', color='#2ca02c', lw=2, label=
        'Kamenetzky model')

    plt.xlabel(r'$\nu$ [GHz]')
    plt.ylabel('Flux [Jy]')
    plt.legend()
    plt.tight_layout()
    plt.show()

    # Walker and trace plots
    fig, axes = plt.subplots(len(PRIOR), 1, figsize=(8, 2 * len(PRIOR)), sharex=
        True)
    samples = sampler.get_chain()
    for i, (ax, key) in enumerate(zip(axes, PRIOR.keys())):
        ax.plot(samples[:, :, i], 'k', alpha=0.3)
        ax.set_ylabel(key)
    axes[-1].set_xlabel('MCMC step')
    plt.show()

if __name__ == '__main__':
```

```
214     if not os.path.isabs(ROOT):
215         script_dir = os.path.dirname(os.path.abspath(__file__))
216         ROOT = os.path.join(os.path.dirname(script_dir), ROOT)
217 
218     print(f"Looking for data in: {ROOT}")
219     try:
220         obs_folders = os.path.join(ROOT, "stacked")
221         run(obs_folders)
222     except Exception as e:
223         print(f"Error: {e}")
224         import traceback; traceback.print_exc()
225         sys.exit(1)
```

Listing A.1: Python script for fitting continuum model of Kamenetzky using its priors ad MCMC

B

Line fitting code

```python
import os
import numpy as np
import matplotlib.pyplot as plt
from scipy.optimize import curve_fit
from scipy.special import wofz
from scipy.interpolate import interp1d
import sys

# Add the project root directory to the path to access the Plotting module
sys.path.append(os.path.dirname(os.path.dirname(os.path.abspath(__file__))))
# Import for side effects - this applies matplotlib styling parameters
from Plotting import plot_settings

# Load stacked, continuum-subtracted, SNR-filtered and sigma clipped data
save_dir = os.path.join('Data', 'npys', 'stacked_snr_filtered')
freq     = np.load(os.path.join(save_dir, 'freq_filtered.npy'))
residual = np.load(os.path.join(save_dir, 'avg_flux_minus_cont.npy'))
var      = np.load(os.path.join(save_dir, 'var_flux_minus_cont.npy'))
sigma_fd = np.sqrt(var)

# Load per-channel Q-factor
Q_factor = np.load(os.path.join(save_dir, 'Q_factor_filtered.npy'))
Q_interp = interp1d(freq, Q_factor, bounds_error=False, fill_value='extrapolate')

# load beam parameters for main beam temperature conversion
beam_dir      = os.path.join('Data', 'beam_width')
beam_freqs    = np.load(os.path.join(beam_dir, 'freqs_20240717114731.npy'))
beam_fwhm_maj = np.load(os.path.join(beam_dir, 'fwhm_maj_20240717114731.npy'))
beam_fwhm_min = np.load(os.path.join(beam_dir, 'fwhm_min_20240717114731.npy'))

# Fix NaNs in beam data by using nearest valid values
for arr in (beam_fwhm_maj, beam_fwhm_min):
    mask = np.isnan(arr)
    if mask.any():
        valid = np.where(~mask)[0]
        for i in np.where(mask)[0]:
            arr[i] = arr[valid[np.abs(valid-i).argmin()]]

# Interpolate beam FWHM values
fwhm_maj_interp = interp1d(beam_freqs, beam_fwhm_maj, bounds_error=False,
    fill_value='extrapolate')
fwhm_min_interp = interp1d(beam_freqs, beam_fwhm_min, bounds_error=False,
    fill_value='extrapolate')
```

```
42
43 # Function to calculate beam solid angle in steradians
44 def beam_solid_angle(nu):
45     maj = fwhm_maj_interp(nu) * np.pi / 648000  # Convert FWHM to radians
46     min = fwhm_min_interp(nu) * np.pi / 648000
47     return 1.133 * maj * min
48
49 # Function to convert flux density in Jy to main beam temperature in K
50 def flux_to_temperature(flux_jy, nu_ghz):
51     c, k_B, Jy = 2.998e8, 1.381e-23, 1e-26  # Constants for speed of light,
           Boltzmann, and Jy
52     nu = nu_ghz * 1e9  # Convert GHz to HzΩ
53      = beam_solid_angle(nu_ghz)  # Get the beam solid angle
54     return (c**2) / (2 * k_B * nu**2 * Ω) * (flux_jy * Jy)
55
56 # Voigt model with wofz as Faddeeva function
57 def voigt_model(x, amp, cen, sig):
58     Q = Q_interp(x)  # Get Q-factor at each frequency
59     gamma = cen / (2 * Q)  # Line width
60     sig_v = sig / np.sqrt(2)  # Adjust standard deviation for Voigt profile
61     z = ((x - cen) + 1j * gamma) / (sig_v * np.sqrt(2))  # Complex argument for
           Faddeeva function
62     return amp * np.real(wofz(z)) / (sig_v * np.sqrt(2 * np.pi))
63
64 # Fit settings, define the lines to fit and window for fitting
65 lines = {'CO(2-1)': 230.538, 'CO(3-2)': 345.796}  # in GHz
66 window = 1  # GHz for selecting the fit region
67 c_kms = 2.998e5  # km/s for speed of light
68
69 results = {}
70 fit_models = {}
71 colors = {'CO(2-1)': 'blue', 'CO(3-2)': 'orange'}
72
73 # Plot the data with error bars
74 plt.figure(figsize=(10,5))
75 plt.errorbar(freq, residual, yerr=sigma_fd, fmt='.', c='gray', alpha=0.5,
       markersize=4, label='Data')
76
77 # Loop through each line to fit
78 for name, center in lines.items():
79     mask_fit = (freq >= center - window) & (freq <= center + window)
80     x_fit, y_fit, e_fit = freq[mask_fit], residual[mask_fit], sigma_fd[mask_fit]
81     A0 = y_fit.max()
82
83     # Set initial parameters and bounds for the fit
84     if name == 'CO(2-1)':
85         p0 = [A0, center, 0.25]
86         bounds = ([0, center - 1.5, 0.1], [10 * A0, center + 1.5, 0.3])
87     else:
88         p0 = [A0, center, 0.30]
89         bounds = ([0, center - 1.5, 0.1], [10 * A0, center + 1.5, 0.3])
90
91     # Perform the Voigt fit using curve_fit
92     popt, pcov = curve_fit(voigt_model, x_fit, y_fit,
93                            p0=p0, sigma=e_fit,
94                            absolute_sigma=True,
95                            bounds=bounds, maxfev=5000)
96     amp, nu0, sig = popt
97     amp_err, nu0_err, sig_err = np.sqrt(np.diag(pcov))
98
99     # Calculate peak temperature and its error
```

```
    peak_Tmb = flux_to_temperature(amp, nu0)

    # Numerical perturbation for peak_Tmb error
    peak_Tmb_plus_amp_err = flux_to_temperature(amp + amp_err, nu0)
    peak_Tmb_minus_amp_err = flux_to_temperature(amp - amp_err, nu0)
    delta_Tmb_amp = (peak_Tmb_plus_amp_err - peak_Tmb_minus_amp_err) / 2

    peak_Tmb_plus_nu0_err = flux_to_temperature(amp, nu0 + nu0_err)
    peak_Tmb_minus_nu0_err = flux_to_temperature(amp, nu0 - nu0_err)
    delta_Tmb_nu0 = (peak_Tmb_plus_nu0_err - peak_Tmb_minus_nu0_err) / 2

    peak_Tmb_err = np.sqrt(delta_Tmb_amp**2 + delta_Tmb_nu0**2)

    # Compute velocity sigma + its error
    sigma_v = c_kms * sig / nu0
    sigma_v_err = np.sqrt((c_kms * sig_err / nu0)**2 +
                          (c_kms * sig * nu0_err / nu0**2)**2)

    # Compute FWHM and its error
    fwhm_v = 2 * np.sqrt(2 * np.log(2)) * sigma_v
    fwhm_v_err = 2 * np.sqrt(2 * np.log(2)) * sigma_v_err

    # Overlay of the window fit
    x_win_plot = np.linspace(center - window, center + window, 200)
    y_win_plot = voigt_model(x_win_plot, amp, nu0, sig)
    plt.plot(x_win_plot, y_win_plot, color=colors[name], lw=2,
             label=f"{name} fit window")

    # Integrate over 20 GHz grid for full line
    Agrid = 20
    nu_min = nu0 - Agrid
    nu_max = nu0 + Agrid
    nu_grid = np.linspace(nu_min, nu_max, 2000)
    flux_fit = voigt_model(nu_grid, amp, nu0, sig)
    vel = c_kms * (nu_grid - nu0) / nu0
    idx = np.argsort(vel)

    I_Jykms = np.trapezoid(flux_fit[idx], vel[idx])
    rel_err = np.sqrt((amp_err / amp)**2 + (sig_err / sig)**2)
    err_Jykms = I_Jykms * rel_err

    Tmb_per_Jy = flux_to_temperature(1.0, nu0)
    I_mKkms = I_Jykms * Tmb_per_Jy * 1e3
    err_mKkms = err_Jykms * Tmb_per_Jy * 1e3

    # Overlay the full 20 GHz fit curve
    plt.plot(nu_grid, flux_fit, color=colors[name], ls='--', lw=1.5,
             label=f"{name} fit σ±5")

    # Store results
    results[name] = {
        'amp (Jy)': (amp, amp_err),
        'cen (GHz)': (nu0, nu0_err),
        'sig (GHz)': (sig, sig_err),
        'σ_v (km/s)': (sigma_v, sigma_v_err),
        'FWHM (km/s)': (fwhm_v, fwhm_v_err),
        'I [Jy·km/s]': (I_Jykms, err_Jykms),
        'I [mK·km/s]': (I_mKkms, err_mKkms),
        'SNR': amp / amp_err,
        'Peak T_mb (K)': (peak_Tmb, peak_Tmb_err)
    }
```

```
    fit_models[name] = popt

    # Print results
    print(f"\n{name} @ {center} GHz:")
    print(f"  Peak T_mb = {peak_Tmb:.2f} ± {peak_Tmb_err:.4f} K")
    print(f"  Amp       = {amp:.3f} ± {amp_err:.3f} Jy")
    print(f"  Cen       = {nu0:.4f} ± {nu0_err:.4f} GHz")
    print(f" σ _v       = {sigma_v:.5f} ± {sigma_v_err:.1f} km/s")
    print(f"  FWHM_v    = {fwhm_v:.5f} ± {fwhm_v_err:.1f} km/s")
    print(f" ∫ flux     = {I_mKkms:.1f} ± {err_mKkms:.1f} mK·km/s")
    print(f"  SNR       = {amp / amp_err:.2f}")

# Plotting
plt.xlabel('Frequency (GHz)')
plt.ylabel('Flux density (Jy/beam)')
#plt.title('Voigt Fits (±1GHz window, σ±5 integration)')
#plt.legend()
plt.grid(alpha=0.3)
plt.tight_layout()
plt.show()
```

Listing B.1: Python script for fitting bright lines using the voigt model

C

Individual observation runs

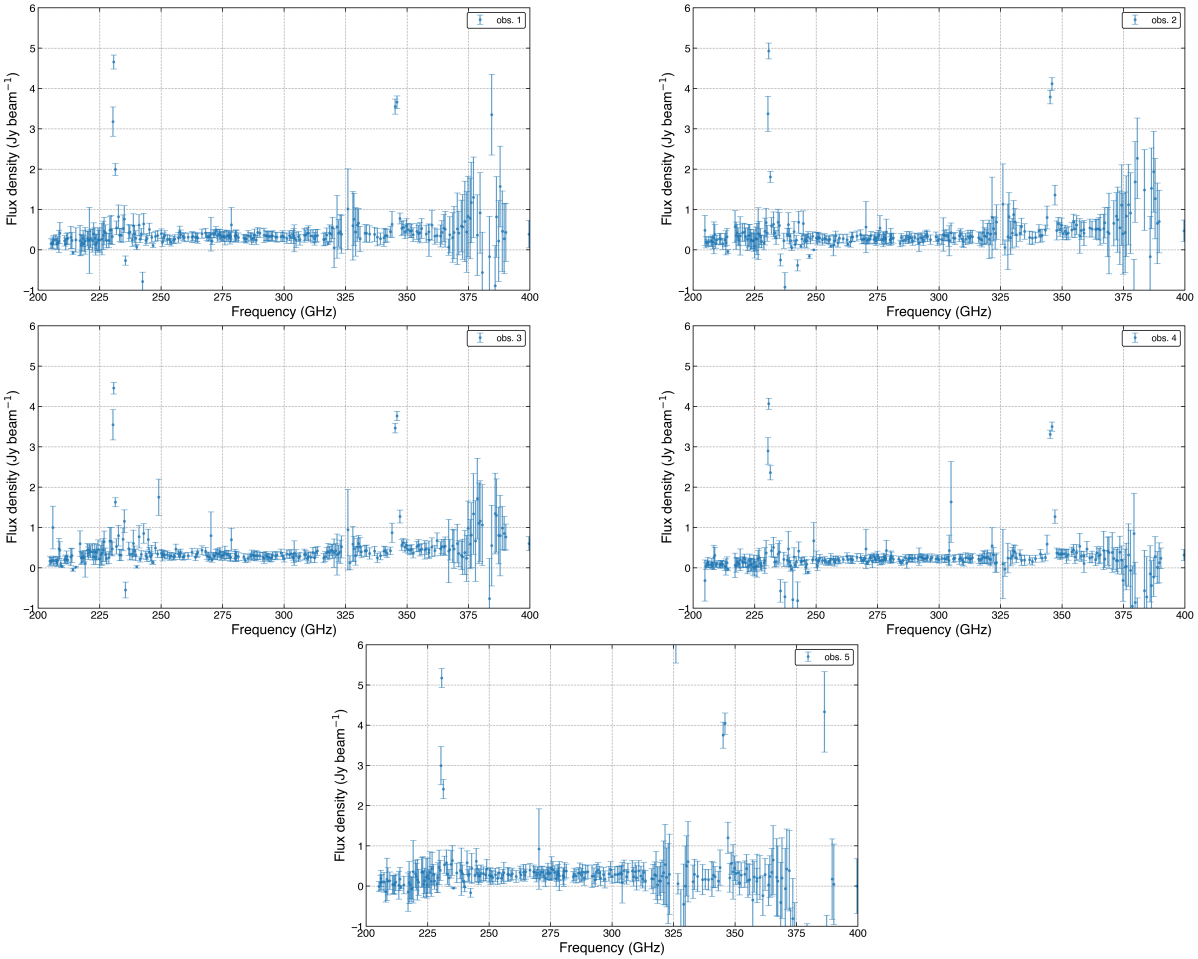

Figure C.1: The five representive observation runs on NGC 1068 as mentioned in the method section

D

Q-factor and Apperture efficiency

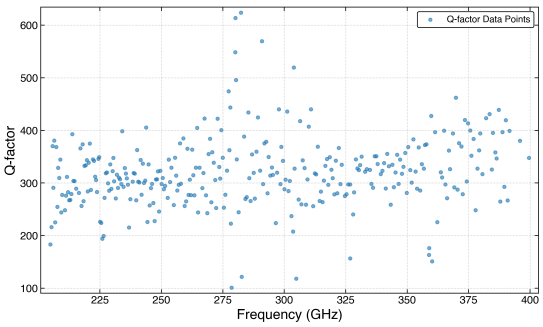

(a) Q factor for each frequency used for line fitting

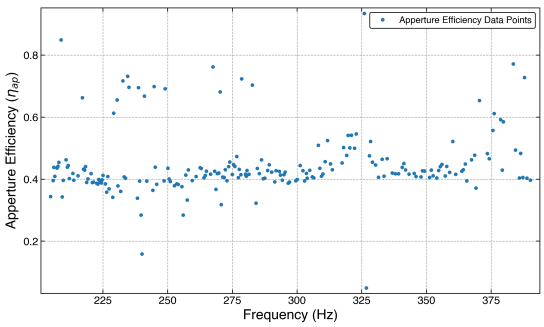

(b) Aperture efficiency used for channels/frequencies

E

Relevant equations

$$I_{\text{K km/s}} = \left(\int F_v, dv \right) \times T_{\text{mb per Jy}} \tag{E.1}$$

$$\text{FWHM}_{\text{km/s}} = c \frac{\text{FWHM}_{\text{GHz}}}{\nu_0} \tag{E.2}$$